ARTICLE

αv-Class integrin binding to fibronectin is solely mediated by RGD and unaffected by an RGE mutation

María Benito-Jardón[1,2]*, Nico Strohmeyer[3]*, Sheila Ortega-Sanchís[1,2], Mitasha Bharadwaj[3], Markus Moser[4], Daniel J. Müller[3], Reinhard Fässler[4], and Mercedes Costell[1,2]

Fibronectin (FN) is an essential glycoprotein of the extracellular matrix; binds integrins, syndecans, collagens, and growth factors; and is assembled by cells into complex fibrillar networks. The RGD motif in FN facilitates cell binding- and fibrillogenesis through binding to α5β1 and αv-class integrins. However, whether RGD is the sole binding site for αv-class integrins is unclear. Most notably, substituting aspartate with glutamate (RGE) was shown to eliminate integrin binding in vitro, while mouse genetics revealed that FN^RGE preserves αv-class integrin binding and fibrillogenesis. To address this conflict, we employed single-cell force spectroscopy, engineered cells, and RGD motif–deficient mice (Fn1^ΔRGD/ΔRGD) to search for additional αv-class integrin–binding sites. Our results demonstrate that α5β1 and αv-class integrins solely recognize the FN-RGD motif and that αv-class, but not α5β1, integrins retain FN-RGE binding. Furthermore, Fn1^ΔRGD/ΔRGD tissues and cells assemble abnormal and dysfunctional FN^ΔRGD fibrils in a syndecan-dependent manner. Our data highlight the central role of FN-RGD and the functionality of FN-RGE for αv-class integrins.

Introduction

Fibronectin (FN) is a glycoprotein of the ECM that is widely expressed in vertebrates throughout all stages of life and assembled by cells into a fibrillar network (McDonald, 1988; George et al., 1993; Mao and Schwarzbauer, 2005). FN fibrils facilitate numerous cellular functions, including cell adhesion, spreading, migration, growth, and survival. The diverse functions of FN are indispensable for mammalian development (George et al., 1993; Georges-Labouesse et al., 1996) and affect diseases such as inflammation, fibrosis, and metastasis (Erdogan et al., 2017). The properties of FN are also used in regenerative medicine, where full-length FN, FN fragments, or FN peptidomimetica serve as substrates for bio-inspired materials (Salmerón-Sánchez et al., 2011; Marín-Pareja et al., 2015). FN is a modular protein composed of three types of folding units (type I, II, and III), which contain interaction motifs for cell adhesion molecules, including integrins and syndecans.

Syndecans consist of four members (syndecan 1–4), bind the heparin II region located within the 12th to 14th FN type III repeats (FNIII12-14; Woods et al., 2000; Mahalingam et al., 2007),

colocalize with integrins in focal adhesions (FAs), and cooperate with integrins to promote F-actin assembly, mechano-transduction, and integrin recycling (Morgan et al., 2007; Chronopoulos et al., 2020). Syndecans binding to FN promote the formation of integrin-containing FAs (Woods and Couchman, 1994; Bloom et al., 1999; Roper et al., 2012; Bass et al., 2011). The major FN-binding cell surface receptors are integrins, which bind different sites in FN. A central cell binding site is the Arg-Gly-Asp (RGD) motif in FNIII10 recognized by several integrins, including α5β1, αIIbβ3 (exclusively expressed on platelets), and αv-class integrins (Leiss et al., 2008). Integrin binding to FN-RGD unfolds soluble FN, aligns, and allows cross-links of FN molecules into fibrils, which are further assembled into a complex network (Mao and Schwarzbauer, 2005; Singh et al., 2010). The FN matrices serve as mold for several FN-binding ECM proteins, including collagens, fibrillin, fibulin, latent TGF-β binding protein (LTBP), perlecan (Pln), and tenascin-C, which incorporate into this complex, 3D ECM mesh (Chung and Erickson, 1997; Twal et al., 2001; Dallas et al., 2005;

[1]Department of Biochemistry and Molecular Biology, Universitat de València, Burjassot, Spain; [2]Institut Universitari de Biotecnologia i Biomedicina, Universitat de València, Burjassot, Spain; [3]Eidgenössische Technische Hochschule Zürich, Basel, Switzerland; [4]Max Planck Institute of Biochemistry, Martinsried, Germany.

*M. Benito-Jardón and N. Strohmeyer contributed equally to this paper; Correspondence to Mercedes Costell: mercedes.costell@uv.es; M. Benito-Jardón's present address is Francis Crick Institute, London, UK; M. Moser's present address is Center for Translational Cancer Research, TUM School of Medicine, Technische Universität München, Munich, Germany.

Kadler et al., 2008; Sottile and Hocking, 2002). Genetic experiments in mice revealed that loss of either α5 or αv integrin expression still allowed the assembly of FN fibrils to proceed in vivo (Yang et al., 1993; Yang and Hynes, 1996; Bader et al., 1998), while adhesion dynamics, integrin signaling, actin morphology, and mechanotransduction were impaired (Wennerberg et al., 1996; Schiller et al., 2013; Strohmeyer et al., 2017). The simultaneous disruption of *Itga5* (encoding integrin α5) and *Itgav* (encoding integrin αv) genes in mice markedly reduced FN expression as well as FN fibril formation and caused lethality at approximately embryonic day 7.5 (E7.5) to E8.0 (Yang et al., 1999). In an attempt to test whether similar defects arise in mice carrying a dysfunctional RGD motif in FN, the aspartate residue of the RGD motif was substituted with a glutamate to produce an RGE (FN^{RGE}), which has been extensively used as an α5β1 and αv-class integrin binding–deficient motif in in vitro experiments (Greenspoon et al., 1993; Beumer et al., 2000; Shiokawa et al., 1999; Leyton et al., 2001; Lee et al., 2019; Niederlechner et al., 2012). Contrary to expectations, these mutant mice produced an apparently normal fibrillar FN network in tissues and developed the same defects as α5-null mice (Takahashi et al., 2007; Yang et al., 1993; Girós et al., 2011), which was regarded as evidence for the existence of a so far unrecognized αv-class integrin binding site in FN. Cellular and biochemical experiments assigned this new αv-class integrin binding to an isoDGR motif in FNI5 (Curnis et al., 2006; Takahashi et al., 2007), which was later shown, however, to lack the capacity to mediate cell adhesion and fibrillogenesis (Xu et al., 2010). Therefore, how αv-class integrin bind and enable cell adhesion to FN^{RGE} both in vitro and in vivo is still an open question.

Here, we use atomic force microscopy–based single-cell force spectroscopy (SCFS), mouse genetics, cell biology, and protein engineering to show that the elimination of the entire RGD motif in FN (FN$^{\Delta RGD}$) disrupts FN binding to both α5β1 and αv-class integrins in vitro and causes defects in vivo that are more severe than in *Fn1$^{RGE/RGE}$* mice and closely resemble those reported for mice lacking the *Fn1* gene. Our experiments also reveal that the aspartate substitution in the RGD motif of FN with a glutamate (RGD>RGE) abolishes α5β1 integrin binding but does not impair αv-class integrin–mediated cell adhesion and spreading. Our results underscore the extraordinary importance of the RGD motif in FN and, unexpectedly, unveil that the RGD>RGE mutation can direct cellular behavior by restricting integrin choice.

Results

The RGD motif in FN is the sole binding site for αv-class integrins

To investigate whether the RGD motif is essential for integrins to bind FN, we used full-length and recombinant fragments of FN with and without mutations in the RGD motif for SCFS experiments with engineered fibroblasts expressing distinct FN-binding integrins. The cell-derived FN (cFN) was purified from the culture medium of wild-type (producing cFN^{RGD}) or *Fn1$^{\Delta RGD/\Delta RGD}$* (producing RGD-deleted cFN [cFN$^{\Delta RGD}$]) fibroblasts (see Materials and methods) and recombinantly expressed FN

fragments containing the 7th to 10th type III repeats (FNIII7-10), which minimized integrin-unspecific interactions in single-cell adhesion experiments. The following FNIII7-10 fragments were expressed: an RGD-deleted fragment (FNIII7-10$^{\Delta RGD}$), a fragment carrying an aspartate-to-glutamate substitution (FNIII7-10^{RGE}), and the unmodified fragment (FNIII7-10^{RGD}) as control. To quantify ligand binding properties of αv-class and α5β1 integrins to cFNs and FNIII7-10 variants by SCFS, we attached single pan-integrin–deficient fibroblasts (pan-integrin KO [pKO]; Schiller et al., 2013) reconstituted with either αv-class (pKO-αv; expressing αvβ3 and αvβ5 integrins) or β1 (pKO-β1; expressing α5β1 integrins) or both classes of integrins (pKO-αv/β1) to concanavalin A–coated cantilevers and performed SCFS with single-molecule sensitivity. Thereto, we lowered cantilever-bound pKO, pKO-αv, pKO-β1, or pKO-αv/β1 fibroblasts onto different cFNs or FNIII7-10 fragments until a contact force of 200 pN was reached and instantly retracted fibroblasts from the substrate, which resulted in a total contact time of ~50 ms (Materials and methods and Fig. S1, a–d). For each cantilever-bound fibroblast, this experiment was repeated multiple times, and the binding probability was calculated as ratio of force–distance (FD) curves showing single unbinding events and all attempts. As expected, pKO fibroblasts showed nonspecific binding probabilities to all tested substrates (Fig. 1, a and b). In line with earlier reports (Benito-Jardón et al., 2017; Bharadwaj et al., 2017), pKO-β1 fibroblasts showed a slightly but nonsignificantly higher binding probability to cFN^{RGD} and FNIII7-10^{RGD} compared with cFN$^{\Delta RGD}$ and FNIII7-10$^{\Delta RGD}$ and nonspecific binding probabilities to FNIII7-10^{RGE} (Fig. 1, a and b). On the contrary, pKO-αv fibroblasts showed comparably high binding probabilities to cFN^{RGD}, FNIII7-10^{RGD}, and FNIII7-10^{RGE} and nonspecific binding probabilities to cFN$^{\Delta RGD}$ and FNIII7-10$^{\Delta RGD}$ (Fig. 1, a and b). Expectedly, pKO-αv/β1 fibroblasts showed the same binding probabilities as pKO-αv fibroblasts to all FNIII7-10 fragment variants (Fig. 1, a and b). Importantly, pKO-αv, pKO-β1, and pKO-αv/β1 fibroblasts showed the same nonspecific binding probabilities to cFN$^{\Delta RGD}$ and FNIII7-10$^{\Delta RGD}$ as pKO fibroblasts, indicating that neither α5β1 nor αv-class integrins bind to RGD-deleted FN within the short contact time (Fig. 1, a and b). To test whether low integrin binding probabilities to FN account for lack of FN binding, we increased the contact time between cantilever-bound cells and FNIII7-10 fragments in binding probability experiments to ~300 ms (Fig. 1 c). The binding probabilities of all pKO-fibroblast lines to FNIII7-10$^{\Delta RGD}$ were not affected by the increased contact time. However, pKO-αv and pKO-αv/β1 fibroblasts displayed an increased binding probability to FNIII7-10^{RGD} and FNIII7-10^{RGE}, whereas the binding probability of pKO-β1 fibroblasts increased only for FNIII7-10^{RGD} and remained at nonspecific levels for FNIII7-10^{RGE} similar to FNIII7-10$^{\Delta RGD}$ (Fig. 1 c). Additionally, experiments with specific integrin–FN interactions revealed in ~25% of all binding probability experiments multiple unbinding events in one experiment, indicating that the ~300-ms time span is sufficiently long for multiple integrins to bind their ligand (Fig. 1 d and Fig. S1 e). Altogether, our experiments show that the RGD motif is essential for αv-class and α5β1 integrins to bind FN and that binding of αv-class integrins to FN^{RGE} is not
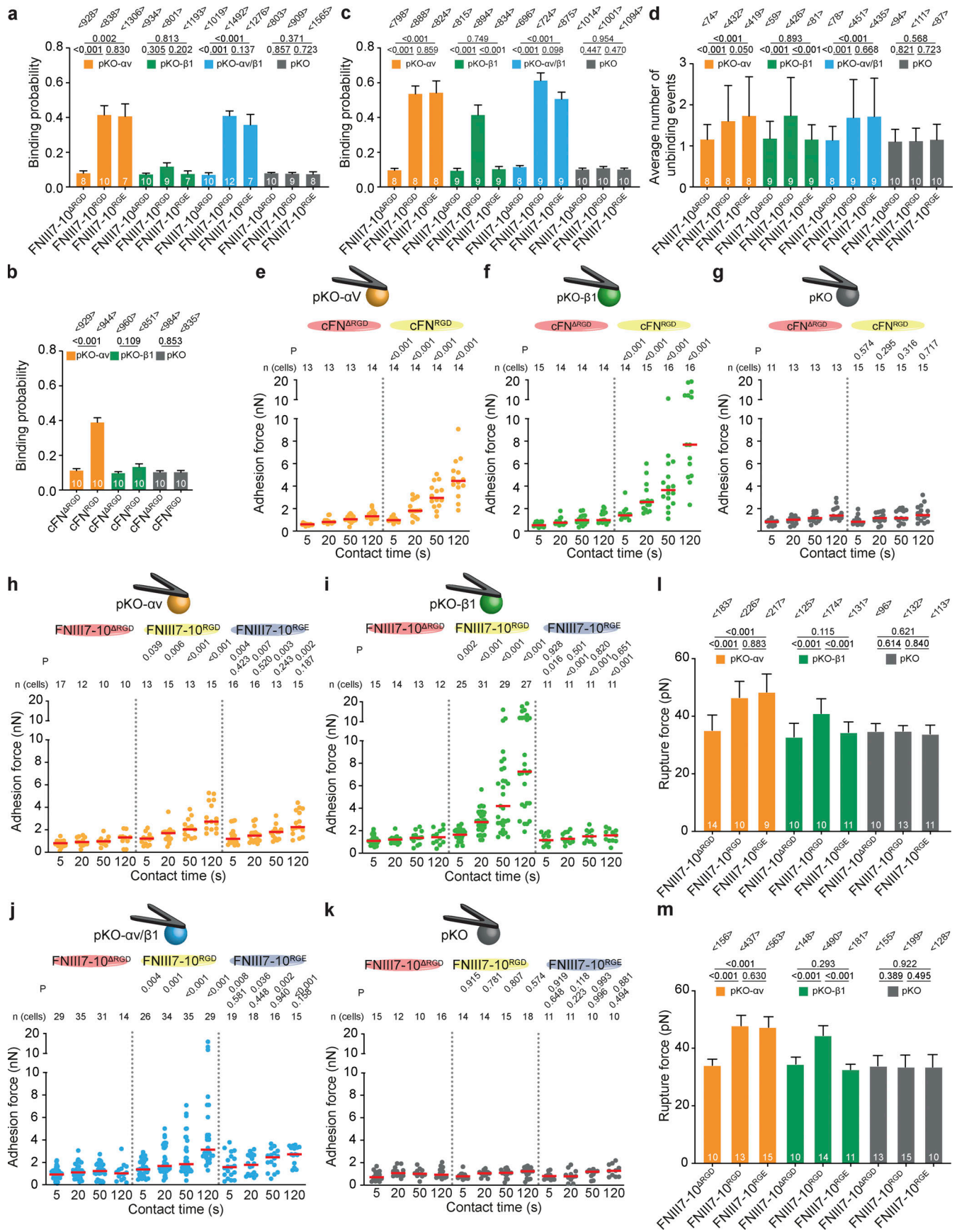
Figure 1.   **The FN-RGD motif is the exclusive binding site for α5β1 and αv-class integrins.** SCFS measurements of pKO, pKO-αv, pKO-β1, and pKO-αv/β1 fibroblasts adhering to different FNIII7-10 fragments and full-length cFN. **(a)** Binding probabilities determined after pKO, pKO-αv, pKO-β1, and pKO-αv/β1 fibroblast contact with FNIII7-10^{RGD}, FNIII7-10^{RGE}, or FNIII7-10^{ΔRGD} fragments for ∼50 ms with a contact force of 200 pN. Adhesion probability was calculated as the ratio of FD curves showing unbinding events and total number of recorded FD curves. n in bars give the numbers of individual fibroblasts tested and <n> the total number of recorded FD curves in each condition. Bars depict mean ± SEM of binding probabilities. P values are given on top of lines that indicate compared conditions. **(b)** Binding probabilities of pKO, pKO-αv, or pKO-β1 fibroblasts to cFN^{RGD} or cFN^{ΔRGD} as described for panel a. **(c)** Binding probability of pKO, pKO-αv, pKO-β1, and pKO-αv/β1 fibroblasts determined after fibroblasts contacted FNIII7-10^{RGD}, FNIII7-10^{RGE}, or FNIII7-10^{ΔRGD} fragments for ∼300 ms with a contact force of 200 pN. Data representation as described for panel a. **(d)** Average number of unbinding events per FD curve acquired for c. Only FD curves showing unbinding events were considered. Data representation as described for panel a. **(e–g)** Adhesion forces of single pKO-αv (e), pKO-β1 (f), or pKO (g) fibroblasts to cFN^{ΔRGD} or cFN^{RGD} after a given contact time are shown as dots and their median as a red bar. P values are given for statistical significance between adhesion forces to cFN^{RGD} and cFN^{ΔRGD} at the indicated contact times. n (cells) gives the number of fibroblasts tested for each condition. **(h–k)** Adhesion forces of single pKO-αv (h), pKO-β1 (i), pKO-αv/β1 (j), or pKO (k) fibroblasts to FNIII7-10^{ΔRGD}, FNIII7-10^{RGD}, or FNIII7-10^{RGE} after given contact times shown as dots and their median as a red bar. Top P values are given for statistical significance between adhesion forces to FNIII7-10^{RGD} and FNIII7-10^{ΔRGD}, and bottom P values are given for comparison of FNIII7-10^{RGD} and FNIII7-10^{RGE} at the indicated contact times. n (cells) gives the number of fibroblasts tested for each condition. **(l and m)** Rupture forces of single ruptures extracted from FD curves after 5-s (l) or 120-s (m) contact times (FD curves are taken from data presented in h, i, and k). Bars are medians and error bars with 95% confidential intervals. All statistical significances were calculated using two-tailed Mann-Whitney test.

compromised, while binding of α5β1 integrin to FN^{RGE} is abrogated.

Adhesion strengthening of αv-class integrins remains unaffected by RGE substitution

To test how the loss of the RGD motif or the D>E substitution influences the adhesion strengthening of αv-class and α5β1 integrins to FN, we quantified adhesion forces of the pKO fibroblast lines to cFNs and FNIII7-10 variants by increasing contact times stepwise from 5 to 120 s (Fig. 1, e–k). In line with previous reports (Spoerri et al., 2020; Strohmeyer et al., 2017; Bharadwaj et al., 2017), pKO-αv, pKO-β1, or pKO-αv/β1 fibroblast lines readily initiated and strengthened adhesion to cFN^{RGD} and FNIII7-10^{RGD} with characteristic integrin-specific dynamics (Fig. 1, e–k; Fig. S1, f and g; and Table S1). Thereby, α5β1 integrins, when expressed alone, strengthened adhesion faster than αv-class integrins alone or when coexpressed with αv-class integrins, which, in the latter case, is due to the out-competition of α5β1 integrins by αv-class integrins (Bharadwaj et al., 2017). Importantly, adhesion forces of pKO-αv, pKO-β1, or pKO-αv/β1 fibroblasts to cFN^{ΔRGD} and FNIII7-10^{ΔRGD} were reduced to nonspecific levels and did not strengthen with increasing contact times, confirming that the RGD motif is essential for integrin-mediated adhesion initiation and strengthening to FN (Fig. 1, e–k; Fig. S1, f and g; and Table S1). Further, pKO-αv and pKO-αv/β1 fibroblasts showed integrin-dependent adhesion forces on FNIII7-10^{RGE} that were similar to those on FNIII7-10^{RGD}, while pKO-β1 fibroblasts exhibited nonspecific adhesion at all contact times (Fig. 1, h–k). Interestingly, the adhesion-strengthening dynamics of pKO-αv and pKO-αv/β1 fibroblasts were not affected on FNIII7-10^{RGE} (Fig. S1 g).

From FD curves, we extracted rupture forces of single unbinding events after 5 s (Fig. 1 l and Fig. S1 d) or 120 s (Fig. 1 m) contact times. We found αv-class integrins showed similar rupture forces during detachment from FNIII7-10^{RGD} and FNIII7-10^{RGE} fragments at either contact time that were significantly higher than those from FNIII7-10^{ΔRGD}. The rupture forces of α5β1 integrins on pKO-β1 fibroblasts, however, were significantly lower during detachment from FNIII7-10^{RGE} compared with FNIII7-10^{RGD} at both 5 s and 120 s contact times and similar

to those recorded for FNIII7-10^{ΔRGD}. Altogether, these results show that (1) α5β1 and/or αv-class integrins require the RGD motif to strengthen cell adhesion, (2) αv-class integrins strengthen adhesion to FN^{RGE} similar to FN^{RGD}, and (3) α5β1 integrins do not bind or strengthen adhesion to FN^{RGE}.

Cell spreading is altered by RGD mutations

To test whether full-length cFN^{RGE} and cFN^{ΔRGD} allows α5β1 and αv-class integrin–mediated adhesion maturation and spreading, we plated pKO-αv, pKO-β1, and pKO-αv/β1 fibroblasts in serum replacement medium (SRM) on purified cFN variants and determined cell spreading as well as morphology and distribution of FAs (Fig. 2). At 60 min after seeding, the great majority of pKO-αv (95.8 ± 4.2%), pKO-β1 (93.1 ± 4.6%), and pKO-αv/β1 (98.0 ± 2.0%) fibroblasts spread on cFN^{RGD}; a slightly lower percentage of pKO-αv (85.0 ± 5.6%) and pKO-αv/β1 fibroblasts (79.6 ± 7.9%) spread on cFN^{RGE}; and a neglectable percentage of pKO-β1 fibroblasts spread on cFN^{RGE}. On cFN^{ΔRGD}, the numbers of spread pKO-αv and pKO-αv/β1 fibroblasts dropped to 22.2 ± 15% and 10.4 ± 7.0%, respectively, and of pKO-β1 fibroblasts to <1% (Fig. 2 a). Moreover, pKO-αv fibroblasts covered less spreading area than pKO-β1 or pKO-αv/β1 fibroblasts on cFN^{RGD} (744 ± 92 μm² versus 897 ± 72 μm², P = 0.022; and 906 ± 72 μm², P = 0.018), similar to pKO-αv (583 ± 42 μm²) and pKO-αv/β1 fibroblasts (514 ± 49 μm²) on cFN^{RGE}. On the contrary, the few adherent pKO-β1 fibroblasts covered a reduced area of 189 ± 29 μm² on cFN^{RGE} (P < 0.001; Fig. 2 b). On cFN^{ΔRGD}, the adherent pKO-αv, pKO-β1, and pKO-αv/β1 fibroblasts covered significantly smaller spreading areas (253 ± 42 μm², 136 ± 8 μm², and 227 ± 27 μm², respectively) when compared with the same cell lines seeded on cFN^{RGD} (Fig. 2 b).

FA and cell morphological parameters were analyzed 90 min after seeding by staining for paxillin and F-actin (Fig. 2 c). Whereas pKO-αv fibroblasts seeded on cFN^{RGD} formed large paxillin-positive FAs at the edges of cellular protrusions, the pKO-β1 and pKO-αv/β1 fibroblasts formed, in addition to the protrusion-located FAs, abundant and small fibrillar adhesions (FBs) that aligned along stress fibers inside the cells. While pKO-αv and pKO-αv/β1 fibroblasts seeded on cFN^{RGE} behaved similarly and developed large FAs at the tips of cellular protrusions but no FBs along stress fibers, clearly resembling the phenotype
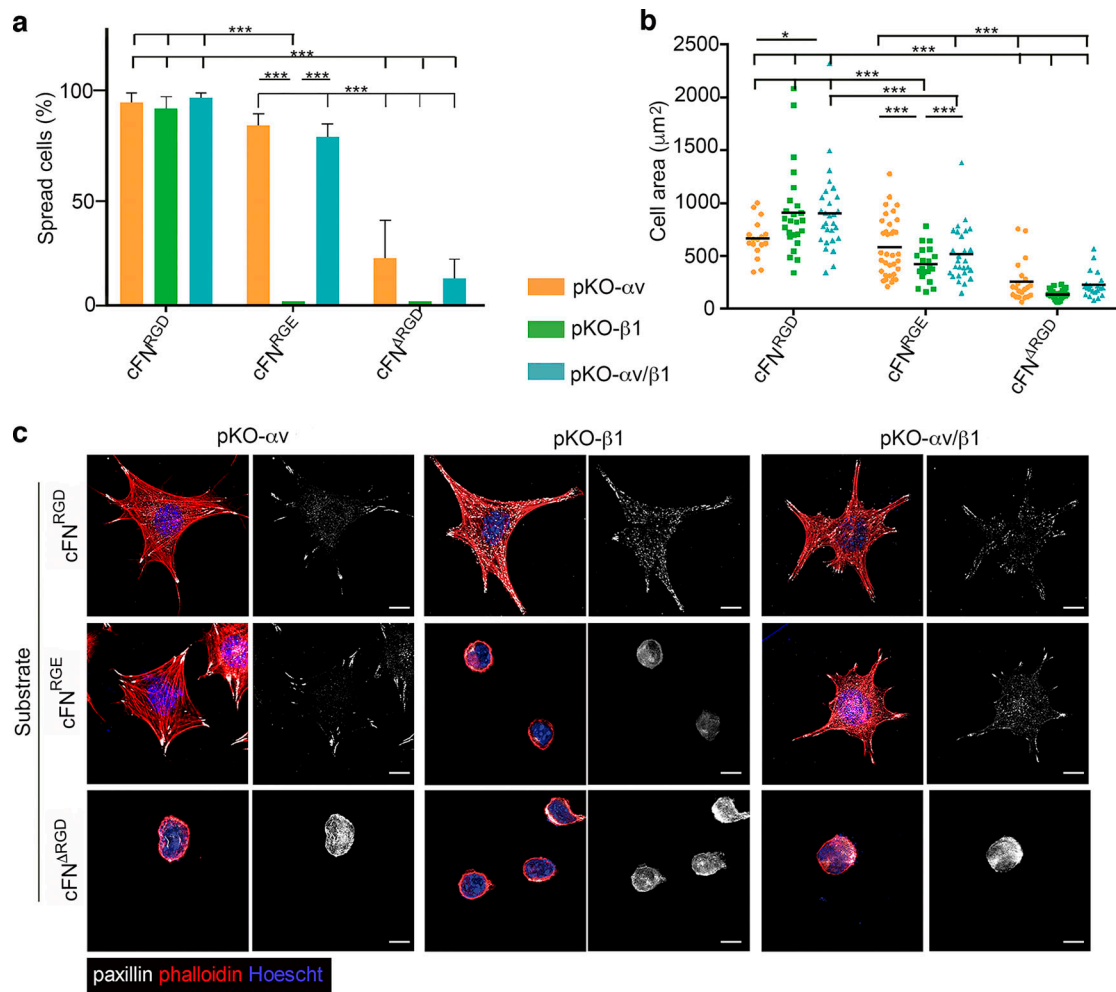
Figure 2. **The FN-RGD motif determines α5β1 and αv -class integrin–mediated fibroblast adhesion and spreading**. **(a)** Percentage of pKO-αv, pKO-β1, and pKO-αv/β1 fibroblasts spread on cFN^{RGD}, cFN^{RGE}, or cFN$^{\Delta RGD}$ after 60-min culture. Bars indicate mean and SD (n = 20–30 cells from three independent experiments). **(b)** Cell area of pKO-αv, pKO-β1, and pKO-αv/β1 fibroblasts seeded on cFN^{RGD}, cFN^{RGE}, or cFN$^{\Delta RGD}$. Lines indicate mean (n = 20–30 cells assessed from three independent experiments). **(c)** Immunofluorescence staining of paxillin (white), F-actin (with phalloidin, red), and nuclei (with DAPI, blue) in pKO-αv, pKO-β1, and pKO-αv/β1 fibroblasts seeded for 90 min on cFN^{RGD}, cFN^{RGE}, or cFN$^{\Delta RGD}$. Statistical significance was calculated using a two-tailed unpaired Student t test; *, P < 0.05; ***, P < 0.001. Scale bars, 10 μm.

of pKO-αv fibroblasts seeded on cFN^{RGD}, the few adherent pKO-β1 fibroblasts on cFN^{RGE} developed neither FAs nor FBs (Fig. 2 c). These findings indicate that the RGE motif abolishes α5β1- but does not compromise αv-class integrin–mediated cellular functions such as FA assembly and spreading.

Lack of the FN-RGD motif arrests development before gastrulation

The findings so far indicate that the absence of the RGD motif is sufficient to abrogate αv-class integrin functions in vitro. To test whether this observation also holds true in vivo, we generated a $Fn1^{\Delta RGD}$ allele by site-directed mutagenesis in embryonic stem (ES) cells and mice (Fig. S2). Heterozygous $Fn1^{\Delta RGD/+}$ mice were viable, fertile, and without an obvious phenotype. Intercrosses of $Fn1^{\Delta RGD/+}$ mice produced no $Fn1^{\Delta RGD/\Delta RGD}$ mice at postnatal day 21. Time-mated heterozygous intercrosses revealed a normal Mendelian distribution of $Fn1^{\Delta RGD/\Delta RGD}$ embryos at E7.5, a reduction from the expected 25% to 20% at E8.5 and 15% at E9.5

(Table 1). The $Fn1^{\Delta RGD/\Delta RGD}$ embryos appeared normal at E7.5, whereas at E8.5, they displayed several pronounced defects, including a shortened anterior–posterior axis, lack of somites, small and distorted headfolds, a small primitive heart bulge, and failure to undergo inside-out turning (Fig. 3 a). At E9.5, the $Fn1^{\Delta RGD/\Delta RGD}$ embryos had still not turned, were severely

Table 1. **Progeny of $Fn1^{+/\Delta RGD}$ intercrosses**

Age	n	$Fn1^{+/+}$ (%)	$Fn1^{+/\Delta RGD}$ (%)	$Fn1^{\Delta RGD/\Delta RGD}$ (%)
E7.5	59	12 (20)	33 (56)	14 (24)[a]
E8.5	102	25 (25)	57 (56)	20 (20)[a]
E9.5	66	16 (24)	40 (61)	10 (15)[b]
E10.5	28	10 (36)	18 (64)	0

[a]All embryos showed a beating heart.
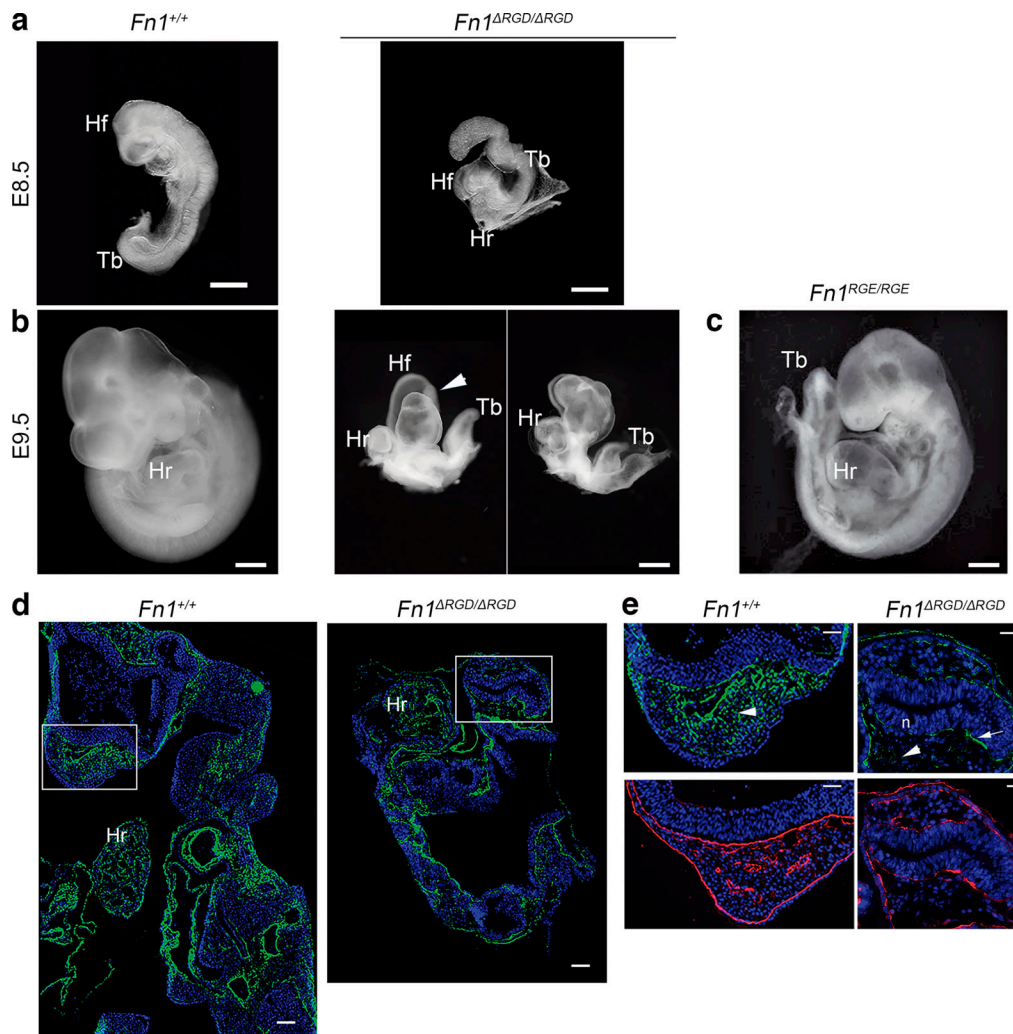[b]Only 5 out of 10 embryos showed a beating heart.

Figure 3.   Development of *Fn1^ΔRGD/ΔRGD* embryos arrests at gastrulation. (a–c) Phenotype of *Fn1^+/+* and *Fn1^ΔRGD/ΔRGD* littermate embryos at E8.5 (a) and E9.5 (b) and for comparison of *Fn1^RGE/RGE* embryo at E9.5 (c). Arrowhead in b points the abnormally shaped telencephalic vesicles. **(d)** FN (green) distribution in E9.5 *Fn1^+/+* and *Fn1^ΔRGD/ΔRGD* embryos. **(e)** Higher magnification of insets depicted in d showing FN and nidogen (red) signals in the telencephalic vesicle and adjacent mesenchyme. Arrowheads in e indicate interstitial tissue and arrow indicates FN in BM of *Fn1^ΔRGD/ΔRGD* embryo. Hf, head folds; Hr, heart; Tb, tail bud. Scale bars, 125 µm (E8.5), 250 µm (E9.5), 200 µm (d), and 50 µm (e).

underdeveloped, lacked somites, and had small heart bulges, and 30% of *Fn1^ΔRGD/ΔRGD* embryos showed also dilated and misshaped head folds (arrowhead in Fig. 3 b). Similar phenotypic defects were also described in embryos with paired null mutations in *It-gav* and *Itga5* genes or with a null mutation in the *Fn1* gene (Yang et al., 1999; George et al., 1993; Georges-Labouesse et al., 1996). Moreover, *Fn1^ΔRGD/ΔRGD* embryos were phenotypically different from *Fn1^RGE/RGE* embryos (Fig. 3 c), which develop the same defects as α5 integrin–deficient mice, including shortened posterior trunk at E9.5, cardiovascular defects, and death at E10–E11 (Takahashi et al., 2007; Girós et al., 2011; Yang et al., 1993). Altogether, these observations indicate that in line with the in vitro experiments, α5β1 as well as αv-class integrins mediate their in vivo functions through binding to the FNIII10-RGD motif.

Fn1^ΔRGD/ΔRGD embryos assemble an aberrant FN^ΔRGD matrix
Since *Fn1^ΔRGD/ΔRGD* and *Fn1^−/−* mice develop similar defects and arrest development before E8.5, we hypothesized that not only

integrin signaling but also the assembly of a FN^ΔRGD matrix are compromised. To test the hypothesis, we immunostained FN in E9.5 embryos and found that FN was widely distributed in both *Fn1^+/+* and *Fn1^ΔRGD/ΔRGD* embryos (Fig. 3 d). A close inspection of consecutively immunostained sections of the telencephalic vesicle for the basement membrane (BM) markers nidogen, laminin, and collagen type IV (Fig. 3 e and Fig. S2 e) revealed that FN was present in BMs as well as interstitial ECM of the *Fn1^+/+* head mesenchyme (arrowhead in Fig. 3 e). In *Fn1^ΔRGD/ΔRGD* embryos, the FN was mostly restricted to BMs, where irregular deposits were apparent (arrow in Fig. 3 e). Interestingly, laminin, nidogen, and collagen type IV showed the same irregular distribution as the FN^ΔRGD (Fig. S2 e). In addition to BMs, tiny, puncta-like FN^ΔRGD deposits were visible in the poorly developed mesenchyme of *Fn1^ΔRGD/ΔRGD* embryos (arrowhead in Fig. 3 e). To exclude that diffusion of maternally derived FN contributes to FN fibril formation in *Fn1^ΔRGD/ΔRGD* embryos, we generated E8.5 *Fn1^−/−* embryos by intercrossing the *Fn1*-floxed allele

([Sakai et al., 2001](#)) with a deletor-Cre transgene, prepared sections, and found, in line with a previous report ([George et al., 1993](#)), that FN deposits were absent from embryonic BMs and interstitial tissues ([Fig. S2, f and g](#)), whereas maternal FN deposits were present in the external layer of the yolk sac (arrow in [Fig. S2 f](#)). These findings indicate that the aberrant and short, puncta-like deposits in tissues of $Fn1^{\Delta RGD/\Delta RGD}$ embryos were not maternally derived.

FN$^{\Delta RGD}$ forms short fibrils in vitro

Although FN fibril formation is thought to be an integrin-dependent process, the lack of α5β1 and αv-class integrin binding to FN$^{\Delta RGD}$ indicates that the fibrils observed in $Fn1^{\Delta RGD/\Delta RGD}$ embryos are formed integrin independently. To further investigate this conundrum, we established $Fn1^{\Delta RGD/\Delta RGD}$ ES cells and fibroblasts to confirm and characterize FN$^{\Delta RGD}$ fibril formation in vitro. As shown in [Fig. 4 a](#), wild-type as well as $Fn1^{\Delta RGD/\Delta RGD}$ ES cell aggregates grown in FN-depleted serum clearly contained FN fibrils, although the FN$^{\Delta RGD}$ fibrils appeared thicker and shorter. The similar expression levels of α5, αv, β1, and β3 and absence of α4 integrin expression on wild-type and $Fn1^{\Delta RGD/\Delta RGD}$ ES cells ([Fig. S3 a](#)) excluded an involvement of α4β1 integrins in FN$^{\Delta RGD}$ fibril formation ([Sechler et al., 2000](#)).

Next, we differentiated $Fn1^{+/+}$ and $Fn1^{\Delta RGD/\Delta RGD}$ ES cells into fibroblasts and established immortalized cell lines that expressed similar levels of α5, αv, β1, and β3 integrins and lacked expression of integrin α4 ([Fig. S3 b](#)). We also excluded α8 integrin subunit expression in pKO ([Schiller et al., 2013](#)), $Fn1^{+/+}$, $Fn1^{RGE/RGE}$ ([Takahashi et al., 2007](#)), and $Fn1^{\Delta RGD/\Delta RGD}$ fibroblasts ([Fig. S3 c](#)) to ensure a faithful comparison of αv-class and α5β1 integrin–mediated FN fibrillogenesis via wild-type or mutant RGD motifs. First, we compared the FN fibrillar network assembled by $Fn1^{+/+}$, $Fn1^{\Delta RGD/\Delta RGD}$, and $Fn1^{RGE/RGE}$ fibroblasts. To this end, we seeded serum-starved cells on laminin, which mediates cell adhesion via α6β1 integrins and leaves αv-class and α5β1 integrins unoccupied and, hence, available for the assembly of self-expressed and secreted FN ([Fig. 4, b and c](#)). 24 h after cell seeding and growing in SRM, the $Fn1^{+/+}$ fibroblasts assembled short FN fibrils and formed characteristic stress fibers that connected paxillin-positive FAs at the cell periphery and aligned with FBs in the cell interior. At 72 h, $Fn1^{+/+}$ fibroblasts assembled long and thin FN fibrils that were distributed in the cell center, and at 120 h after seeding, the FN fibrils increased in length, were denser, and aligned with the actin fibers ([Fig. 4 b](#)). In sharp contrast, $Fn1^{\Delta RGD/\Delta RGD}$ fibroblasts harbored most of their FN in intracellular vesicles, and only very few short and thick fibrils were visible at the cell tips 24 h after seeding. Furthermore, the $Fn1^{\Delta RGD/\Delta RGD}$ fibroblasts contained fewer stress fibers connected to the adhesion sites at the cell periphery, and the majority of paxillin remained diffusely distributed in the cytoplasm. Although at 72 and 120 h after seeding the FN$^{\Delta RGD}$ matrix increased in complexity, the FN fibrils remained short, thick, and located to peripheral adhesions ([Fig. 4 c](#)). Finally, the $Fn1^{RGE/RGE}$ fibroblasts assembled their secreted FN^{RGE} already 24 h after seeding into thin fibrils that were poorly aligned with the stress fibers and mainly located to the cell periphery, forming fibrillar networks that were of lower density than those of $Fn1^{+/+}$ fibroblasts

([Fig. 4 d](#)). To quantify the amount of soluble and of functional FN that is assembled into insoluble cross-linked fibrils, cell cultures were extracted with sodium deoxycholate (DOC), which efficiently separates soluble from insoluble FN. In addition, we also quantified unassembled FN secreted into the conditioned SRM by the cells. Expectedly, $Fn1^{+/+}$ fibroblasts assembled increasing amounts of insoluble fibrils with increasing culturing time, whereas the unassembled FN in the conditioned medium remained low. Consistently with the poor assembly of FN$^{\Delta RGD}$ fibrils, the levels of DOC-extracted, insoluble cross-linked FN$^{\Delta RGD}$ were down to ∼8% in $Fn1^{\Delta RGD/\Delta RGD}$ cells after 5 d in culture ([Fig. 4, e and f](#)), whereas the unassembled FN$^{\Delta RGD}$ increased in the conditioned medium, reaching ninefold-higher levels when compared with $Fn1^{+/+}$ fibroblasts. The FN^{RGE} secreted by $Fn1^{RGE/RGE}$ fibroblasts also accumulated in the conditioned medium to significantly higher amounts than in conditioned medium of $Fn1^{+/+}$ fibroblasts. Importantly, the intracellular, DOC-soluble FN contents in cell extracts were similar in $Fn1^{+/+}$, $Fn1^{RGE/RGE}$, and $Fn1^{\Delta RGD/\Delta RGD}$ fibroblasts at all time points tested ([Fig. 4, e and f](#)), indicating that FN expression is not altered in $Fn1^{RGE/RGE}$ or $Fn1^{\Delta RGD/\Delta RGD}$ cells. To exclude that FN$^{\Delta RGD}$ fibrils are only assembled when fibroblasts are seeded on laminin, we cultured $Fn1^{+/+}$ and $Fn1^{\Delta RGD/\Delta RGD}$ fibroblasts on vitronectin (VN) or collagen type I and found that $Fn1^{\Delta RGD/\Delta RGD}$ fibroblasts formed short and thick FN$^{\Delta RGD}$ fibrils on both substrates ([Fig. S4](#)), although not restricted to the periphery tips, as observed with $Fn1^{\Delta RGD/\Delta RGD}$ fibroblasts seeded on laminin ([Fig. 4 c](#)).

It has been reported that FN fibrils serve as scaffold for several ECM proteins, including collagens and proteoglycans such as Pln ([Kadler et al., 2008](#); [Chung and Erickson, 1997](#)). The Pln matrix assembled by $Fn1^{+/+}$ or $Fn1^{RGE/RGE}$ fibroblasts cultured in SRM on a laminin-coated substrate for 5 d consisted of a similar and elaborated network ([Fig. 4 g](#)). In sharp contrast, the Pln network laid down by $Fn1^{\Delta RGD/\Delta RGD}$ fibroblasts was less dense, and the majority of Pln was inside the cells. These results indicate that FN$^{\Delta RGD}$ fibrils are dysfunctional to nucleate complex ECMs.

The heparan sulfate–binding sites in FN facilitate FN$^{\Delta RGD}$ fibril formation

Our findings demonstrate that αv-class integrins assemble FN^{RGE} exclusively by binding the RGE motif in vitro and in vivo. The assembly of FN$^{\Delta RGD}$ fibrils was unanticipated as FN fibril formation is believed to be integrin driven. Since α4 and α8 integrins are not expressed on $Fn1^{\Delta RGD/\Delta RGD}$ ES cells and fibroblasts ([Fig. S3, a and b](#)) and during early mouse development ([Takahashi et al., 2007](#)), α5β1 and αv-class integrins do not bind FN$^{\Delta RGD}$, and an additional αv-class integrin binding site is not available in FN, we hypothesized that the assembly is most likely orchestrated by nonintegrin cell surface proteins. Potential candidates are members of the syndecan family, which are ubiquitously expressed ([Morgan et al., 2007](#)), bind the heparan sulfate binding motifs of FN, and were shown to promote integrin-induced formation of FN fibrils in vitro ([Stepp et al., 2010](#)). Western blot (WB) analyses revealed the presence of all four syndecans in $Fn1^{+/+}$ as well as $Fn1^{\Delta RGD/\Delta RGD}$ fibroblasts with syndecan 1, 2, and 4 expressed at higher levels by $Fn1^{\Delta RGD/\Delta RGD}$
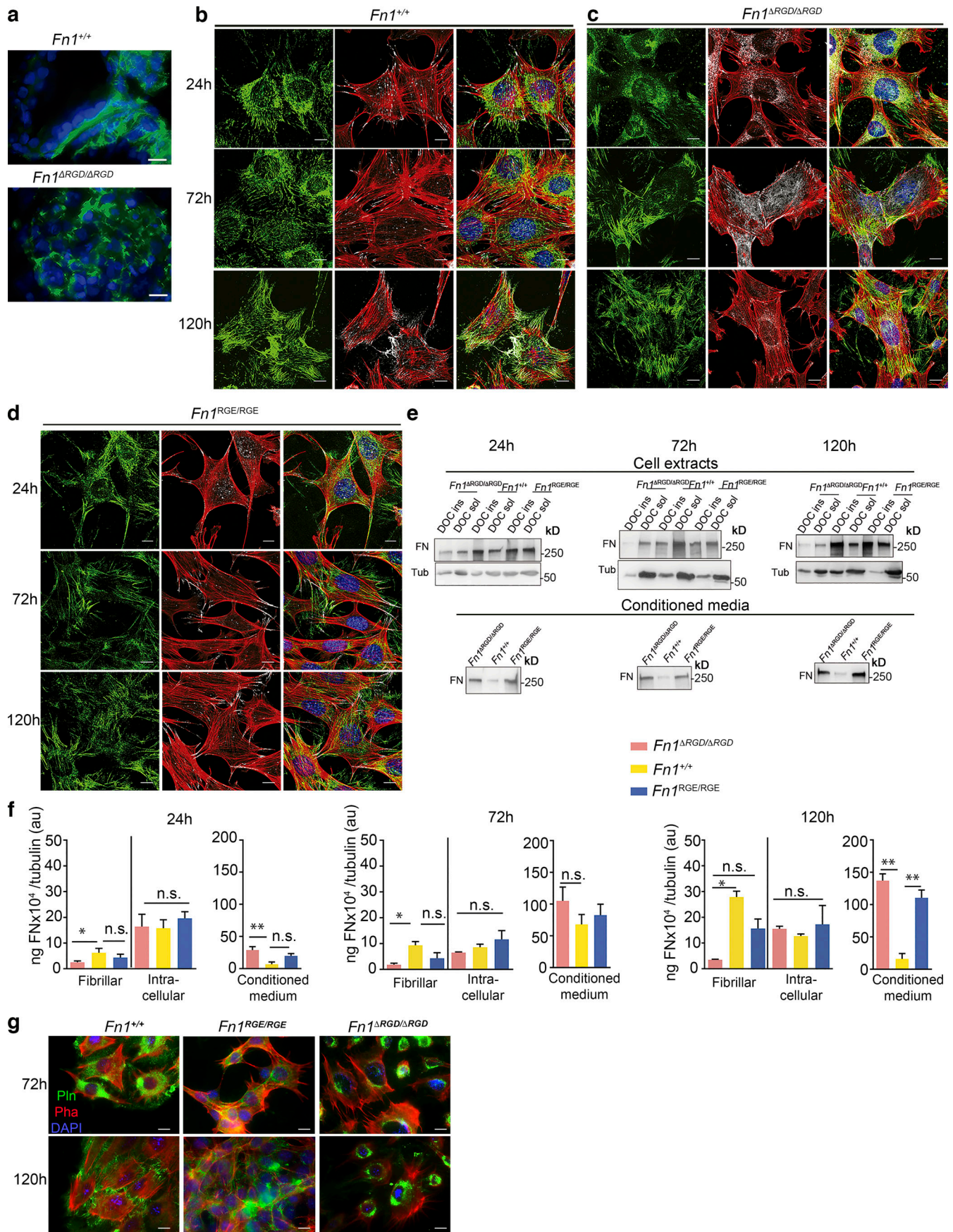
Figure 4.   **FN$^{\Delta RGD}$ is assembled into short and thick fibrils. (a)** Immunofluorescence of FN (green) assembled by $Fn1^{+/+}$ and $Fn1^{\Delta RGD/\Delta RGD}$ ES cell aggregates. **(b–d)** $Fn1^{+/+}$, $Fn1^{\Delta RGD/\Delta RGD}$, and $Fn1^{RGE/RGE}$ fibroblasts seeded on laminin and stained for F-actin (phalloidin; red), paxillin (white), and FN (green) at indicated time points after cell seeding. **(e)** Representative WBs of FN content in whole-cell lysates, including DOC-insoluble and DOC-soluble fractions, and in the conditioned medium. Tub, tubulin. **(f)** Quantification of DOC-insoluble and DOC-soluble FN from cell extracts and FN in the conditioned medium at indicated time points after seeding. FN levels are shown relative to tubulin in the cell extract. au, arbitrary units. Bars indicate mean and SEM of three independent experiments ($n = 3$). Statistical significance was calculated using two-tailed unpaired Student t tests and corrected with a Bonferroni post-hoc test; *, $P < 0.05$; **, $P < 0.01$; n.s., not significant. **(g)** Pln (green) deposition in matrices assembled by $Fn1^{+/+}$, $Fn1^{RGE/RGE}$, and $Fn1^{\Delta RGD/\Delta RGD}$ fibroblasts. Scale bars, 10 µm.

than by $Fn1^{+/+}$ fibroblasts (Fig. 5 a). Flow cytometry analysis confirmed the twofold higher surface expression levels of syndecan 4 on $Fn1^{\Delta RGD/\Delta RGD}$ fibroblasts compared with $Fn1^{+/+}$ fibroblasts (Fig. S3 b). To investigate whether syndecans mediate FN$^{\Delta RGD}$ fibrillogenesis, we cultured cells in SRM and characterized the assembly of self-secreted FN in the presence of heparin (Fig. 5, b and c; and Fig. S5 a), which blocks the heparan sulfate binding motifs on FN and, hence, syndecan binding to FN (Peterson et al., 2005). Whereas $Fn1^{+/+}$ fibroblasts seeded on laminin formed similar FN networks with similar numbers of FN fibril branch points in the presence as well as absence of heparin, $Fn1^{\Delta RGD/\Delta RGD}$ fibroblasts assembled short and thick FN fibrils with significantly fewer branch points (Fig. S5 a), and in the presence of heparin, FN$^{\Delta RGD}$ fibrils were absent and FN$^{\Delta RGD}$ was only visible intracellularly (Fig. 5 c and Fig. S5 a). $Fn1^{\Delta RGD/\Delta RGD}$ fibroblasts treated with heparin were also less spread and accumulated F-actin at the cell cortex. Consistent with the blocking effect of heparin on FN fibrillogenesis by $Fn1^{\Delta RGD/\Delta RGD}$ fibroblasts, significantly less DOC-insoluble FN$^{\Delta RGD}$ was isolated from the heparin-treated cells compared with untreated $Fn1^{\Delta RGD/\Delta RGD}$ fibroblasts (Fig. 5 d). Heparin treatment affected neither the amount of DOC-insoluble FN isolated from $Fn1^{+/+}$ fibroblasts nor from $Fn1^{RGE/RGE}$ fibroblasts (Fig. 5 d and Fig. S5, b and c). Addition of MnCl$_2$ to the cell culture medium, which binds to and activates integrins (Beauvais and Rapraeger, 2010), further confirmed that integrins are not involved in the assembly of FN$^{\Delta RGD}$ fibrils, as heparin treatment blocked FN$^{\Delta RGD}$ fibril formation irrespective of the presence of MnCl$_2$ (Fig. S5 d). Expectedly, MnCl$_2$ induced a robust assembly of FN fibrils in $Fn1^{+/+}$ and $Fn1^{RGE/RGE}$ fibroblasts, both in the presence and absence of heparin.

Next, we directly addressed whether syndecans mediate FN$^{\Delta RGD}$ fibril assembly by depleting syndecan mRNAs in $Fn1^{\Delta RGD/\Delta RGD}$ fibroblasts using siRNAs. Depletion of all four syndecan mRNAs, with four specific siRNAs, compromised $Fn1^{\Delta RGD/\Delta RGD}$ fibroblast survival in SRM. Since the siRNA-mediated depletion of syndecan 1 (sdc1) reduced levels of sdc1 and sdc3 to 60% and the siRNA against syndecan 4 (sdc4) reduced levels of sdc2 and sdc4 to 13–30% in $Fn1^{\Delta RGD/\Delta RGD}$ fibroblasts (Fig. S5, e and f), we combined them to diminish syndecan expression in $Fn1^{\Delta RGD/\Delta RGD}$ and $Fn1^{+/+}$ fibroblasts (Fig. 5 e). Whereas scrambled (scr) siRNA affected neither DOC-insoluble FN levels nor FN^{RGD} and FN$^{\Delta RGD}$ fibril assembly (Fig. 5, f and g) in cell extracts from $Fn1^{+/+}$-scr or $Fn1^{\Delta RGD/\Delta RGD}$-scr fibroblasts, FN$^{\Delta RGD}$ assembly was severely compromised upon syndecan silencing in $Fn1^{\Delta RGD/\Delta RGD}$-sdc-KD, but not in $Fn1^{+/+}$-sdc-KD, fibroblasts,

consolidating that syndecans mediate the aberrant FN$^{\Delta RGD}$ fibrillogenesis (Fig. 5, f and g; and Fig. S5 g).

Discussion

ECMs are organized into complex 3D structures that are essential for morphogenesis and postnatal homeostasis (Wilson et al., 2005). Knowledge of how these complex ECMs are assembled and how cells respond to them is pivotal for the understanding of development and disease and the successful design of bio-inspired materials. FN takes a central role in ECM assembly, as it is thought to serve as a binding platform for several unrelated ECM proteins such as collagens (Kadler et al., 2008), tenascins, Pln, etc. The assembly of FN is a cell- and force-driven process steered by α5β1 and αv-class integrins that bind, unfold, and permit FN cross-linking into a fibrillar network (Pankov et al., 2000; Mao and Schwarzbauer, 2005). A central question is whether αv-class integrins exclusively bind to the RGD motif or whether additional sites in FN (e.g., the NGR motif in FNI5 and other FN modules; Curnis et al., 2006; Takahashi et al., 2007) also serve as binding sites that mediate cell adhesion and drive FN assembly.

To address this question, we used an interdisciplinary approach whose results demonstrate that the RGD motif in FN is, like for α5β1 integrin, also the sole binding motif for αv-class integrins, and, unlike previously thought (Greenspoon et al., 1993; Beumer et al., 2000; Shiokawa et al., 1999; Leyton et al., 2001; Lee et al., 2019; Niederlechner et al., 2012), the substitution of the aspartate with a glutamate (RGD>RGE) in the FN-RGD motif impedes α5β1 integrin binding but leaves binding to αv-class integrins unaffected. Furthermore, we show that FN$^{\Delta RGD}$ is (poorly) assembled into short, thick, and dysfunctional fibrils by syndecans, which bind to the heparin II–binding site in FNIII12-14.

These results clearly indicate that the RGD motif in FN is essential not only for integrin binding and cell adhesion but also for the assembly of a functional FN matrix. SCFS and cell-spreading experiments using different RGD mutations in full-length FNs and pKO cells reconstituted to express either α5β1 and/or αv-class integrins confirmed this conclusion and showed that neither α5β1 nor αv-class integrins can bind to RGD-deleted FN. Whereas the RGD>RGE substitution abrogates binding of α5β1 integrin, αv-class integrins binding to and adhesion strengthening on FNIII7-10^{RGE} occurs normally and is characterized by high on-rate binding events and rupture forces of single unbinding events that are also seen in experiments with FNIII7-10^{RGD} fragments.

In line with our in vitro experiments, $Fn1^{\Delta RGD/\Delta RGD}$ mice develop pronounced morphogenetic defects between E7.5 and E8.5
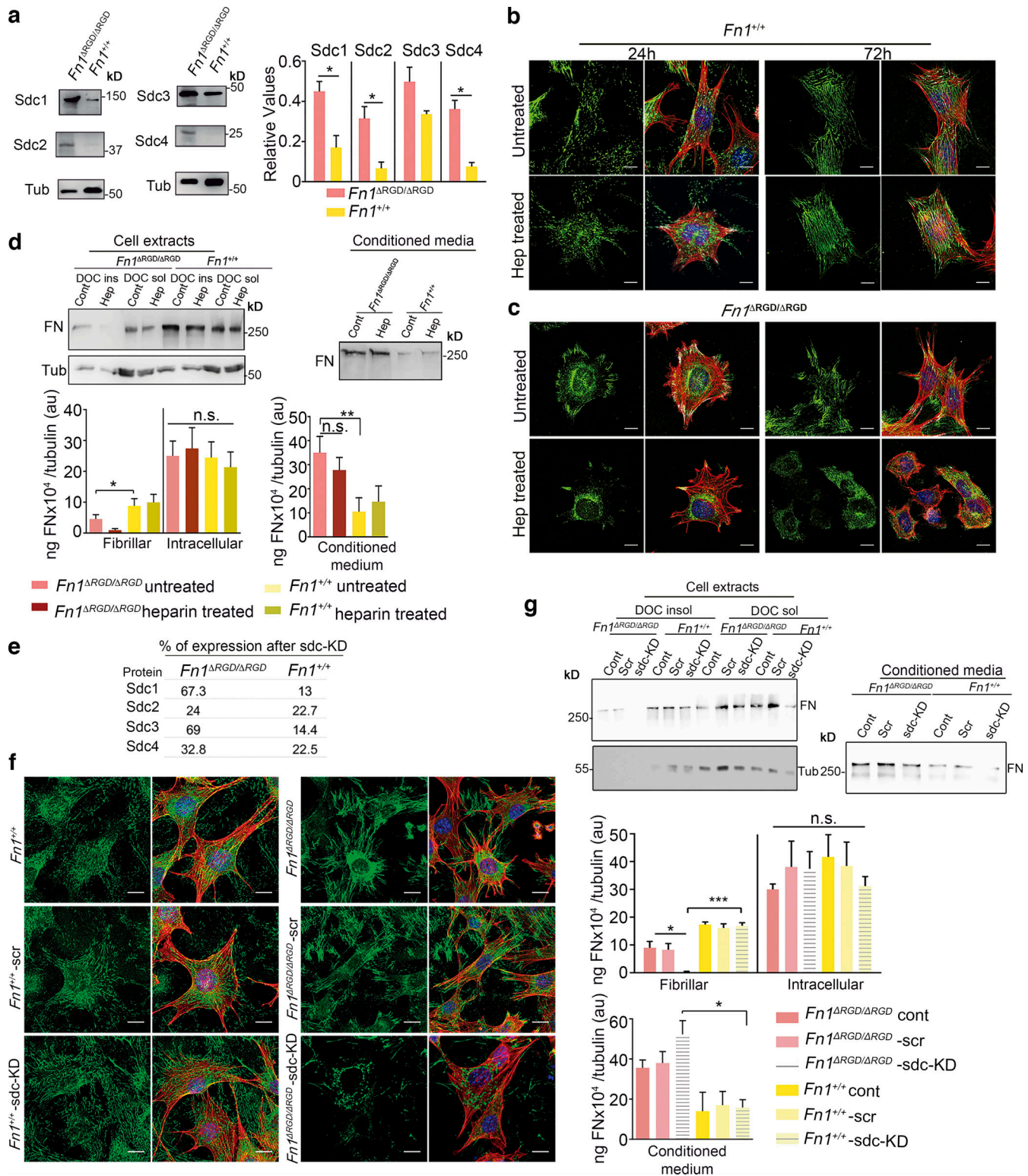
Figure 5. **The heparan sulfate–binding site in FN facilitates FN$^{\Delta RGD}$ fibrillogenesis. (a)** Representative WB of syndecans 1–4 in $Fn1^{+/+}$ and $Fn1^{\Delta RGD/\Delta RGD}$ fibroblasts and quantification of three (n) independent experiments adjusted to tubulin (Tub) levels. Bars indicate mean and SEM. Statistical significance was calculated using a two-tailed unpaired Student t test; *, P < 0.05. **(b and c)** FN assembly by $Fn1^{+/+}$ and $Fn1^{\Delta RGD/\Delta RGD}$ fibroblasts seeded on laminin and treated with heparin (Hep) at the indicated time points. **(d)** Representative WB and quantification of DOC-insoluble and DOC-soluble FN in cell extracts and FN in the conditioned medium without and with heparin treatment for 24 h. **(e)** Percentage of syndecan protein expression in $Fn1^{\Delta RGD/\Delta RGD}$ and $Fn1^{+/+}$ fibroblasts transfected with 150 nM siRNA. **(f)** Fluorescence of FN (green), F-actin (red), and nuclei (DAPI) by indicated fibroblast lines. **(g)** Representative WB and quantification of DOC-insoluble and DOC-soluble FN in cell extracts and FN in the conditioned medium of cells treated with either scr RNA or siRNA. FN levels are shown relative to tubulin in the cell extract. Bars indicate mean SEM of three (n) independent experiments. Statistical significance was calculated using a two-tailed unpaired Student t test and corrected with a Bonferroni post-hoc test; *, P < 0.05; **, P < 0.01; ***, P < 0.001; n.s., not significant. Scale bars in b, c, and f, 10 μm. au, arbitrary units; KD, knockdown.

that are similar to *Itga5/Itgav* double-null mice but differ substantially from those observed in *Fn1^RGE/RGE* mice, which resemble the phenotype of *Itga5*-null mice (Takahashi et al., 2007; Girós et al., 2011; Yang et al., 1993). Together with the in vitro experiments, the phenotype of *Fn1^ΔRGD/ΔRGD* mice confirms the FN-RGD motif to be the sole binding site in FN for both α5β1 and αv-class integrins in vivo. The selective loss of α5β1 binding to FN^RGE observed in SCFS experiments provides an explanation why *Itga5*-null and *Fn1^RGE/RGE* embryos share the same defects (Takahashi et al., 2007; Yang et al., 1993) and raises concerns regarding the RGE-containing FN fragments used in vitro and ex vivo as non–integrin-binding compounds (Beumer et al., 2000; Shiokawa et al., 1999; Leyton et al., 2001). In the *Fn1^ΔRGD/ΔRGD* embryos, we observe a drastic reduction of FN in interstitial tissues that could, at least in part, be due to the defective development of mesoderm, which is also observed in *Itga5/Itgav* double-null embryos and associated with an abnormal development of the telencephalic vesicles and primitive heart. The assembly of FN in interstitial tissues is driven by cell surface receptors. In line with our previous report (Benito-Jardón et al., 2017), we confirm that the synergy site in FNIII9 is insufficient to associate with α5β1 in the absence of the RGD motif, and therefore, α5β1 integrin–synergy site interaction can be excluded as an RGD-independent assembly mechanism. Furthermore, the NGR/isoDGR motif in the FNI5 module, which was shown to bind αvβ3 integrins (Curnis et al., 2006; Takahashi et al., 2007; Curnis et al., 2010) clearly cannot compensate the absence of the RGD motif in FN^ΔRGD for cell adhesion, adhesion strengthening, cell spreading, and development. These findings, together with a report showing that substitution of asparagine (N) in the NGR motif of FNI5 and FNI7 with glutamine (Q) does not prevent fibril formation (Xu et al., 2010), strongly argue against a functional role of FN's NGR motifs. Finally, α4β1, which binds to the variable region of FN and is also able to assemble FN fibrils (Sechler et al., 2000), is not expressed at this stage of development.

These results raised the question of how FN^ΔRGD could be assembled. Syndecans are an alternative family of adhesion molecules that potentially initiate FN assembly. They directly bind to the heparin II domain (FNIII12-14) of FN (Woods et al., 2000; Mahalingam et al., 2007), are expressed on almost all cells (Morgan et al., 2007), colocalize with integrins in FAs, and have been proposed to make the initial contacts with FN (Woods and Couchman, 1994; Bloom et al., 1999). Syndecan 1, for example, has been shown to promote FN assembly through activation of αv-class integrins (Beauvais and Rapraeger, 2010; Yang and Friedl, 2016) or α5β1 cosignaling (Wang et al., 2010), and syndecan 2 to facilitate the assembly of FN fibrils (Galante and Schwarzbauer, 2007; Klass et al., 2000). Our cell culture experiments also reveal the involvement of syndecans in the formation of FN^ΔRGD fibrils. Both addition of heparin to block the syndecan binding site in FN and the depletion of syndecan expression almost completely abrogated FN^ΔRGD fibril assembly. It is possible that the weak interactions of syndecans with the actomyosin cytoskeleton and, hence, transmission of weak pulling forces to the syndecan–FN bonds are sufficient to partially unfold FN^ΔRGD and assemble FN^ΔRGD fibrils that require the input of integrins for further maturation into thick, long, and functional fibrils.

In addition to the small FN^ΔRGD deposits in interstitial tissues of *Fn1^ΔRGD/ΔRGD* embryos, we also observed aberrant FN^ΔRGD deposits in BMs. FN deposition at BMs has recently been shown to be assembled differently from interstitial FN fibrils (Lu et al., 2020). Although the study did not identify how cells initiate FN recruitment, cells generate pulling forces induced by integrins binding to the BM components laminin and collagen IV, initiate FN unfolding, and induce fibril formation, and, as FAs mature, switch to α5β1 integrin binding, which will elongate and move the FN fibrils into the cell center. Interestingly, we also observed that fibroblasts seeded on laminin recruit cFN^ΔRGD to the cell periphery, where it remains and, probably due to the lack of α5β1–FN^ΔRGD interactions, never matures further, elongates, and moves into the cell center. Interestingly, discontinuous FN^ΔRGD deposits also predominate in BMs of *Fn1^ΔRGD/ΔRGD* embryos. Syndecans, which make first contacts with FN, crosstalk with integrins, and modulate integrin functions (Woods and Couchman, 1994; Bloom et al., 1999; Wang et al., 2010; Chronopoulos et al., 2020; Bass et al., 2007), may also serve as initiators of the FN assembly process in BMs.

FN peptides containing an RGE motif are frequently used in control experiments to show that they, in contrast to RGD-containing peptides, do not impair, for example, cell adhesion to FN, or even other ECM proteins containing cell binding RGD motifs (Ruoslahti and Pierschbacher, 1987; Cherny et al., 1993; Greenspoon et al., 1993). It is not clear why the robust binding of αv-class integrins to the RGE motif went unnoticed. A possible explanation is that the FN-RGE peptide–mediated blocking of αvβ3 integrin for FN binding was masked by the high coexpression of other FN-binding integrins such as α5β1 or α4-class integrins, which do not bind FN-RGE and, hence, mask the inhibitory effect for αv integrins. Alternatively, the molecular properties of the used peptides, including their structure and sequences flanking the RGD (or RGE) motif, may have abrogated the recognition by αv-class integrins, which would also explain why the RGD>RGE mutation in VN eliminates αvβ3 and αvβ5 integrin binding (Cherny et al., 1993). Finally, it is also possible that due to the overwhelming literature on a loss of function associated with the RGE motif, potential functional hints of RGE have been overlooked. Nevertheless, our observation reported here opens the opportunity to dictate whether α5β1 and/or αv-class integrins bind FN by substituting the aspartate to glutamate in FN's RGD motif, and to expand the toolbox for designing FN-RGE–containing biomaterials that only allow αv-class integrin engagement or prevent αv-class integrin and favor α5β1 integrin binding to FN-RGD by applying soluble RGE-containing peptidomimetica. This strategy, for example, could direct the differentiation of bipotent pancreatic progenitor cells (Mamidi et al., 2018) into either the duct lineage, by inhibiting αv-class integrins with soluble RGE peptidomimetica, or the hormone-producing cell lineage, by exclusively engaging αv-class integrins. Further interesting applications include regulating osteoclasts and bone resorption (Nakamura et al., 2007), angiogenesis (Lovett et al., 2009; Korntner et al., 2019), or cancer progression

(Kozlova et al., 2001) through the specific engagement or inhibition of αv-class integrins to FN.

Materials and methods

Production of the FNIII7-10 fragments

We subcloned the human cDNA encoding FNIII7-10 in the expression vector pET-15b (Takahashi et al., 2007). The substitution of D to E or deletion of the entire RGD motif was achieved by site-directed mutagenesis and allowed expression of FNIII7-10^{RGE} or FNIII7-10$^{\Delta RGD}$ fragments, respectively, in the *Escherichia coli* strain Rosetta T1R. The fragments were purified using TALON Metal Affinity chromatography (Clontech) and gel filtration chromatography using Superdex 200 10/300 GL columns (GE Healthcare) and eluted in PBS.

SCFS

For cell attachment, cantilevers were plasma cleaned (PDC-32G; Harrick Plasma) and then incubated overnight at 4°C in PBS containing concanavalin A (2 mg/ml; Sigma-Aldrich; Friedrichs et al., 2013). For substrate coatings, a 200-µm-thick four-segmented polydimethylsilane mask fused to the surface of glass-bottom Petri dishes (WPI) was used (Yu et al., 2015). Each of the four polydimethylsilane-framed glass surfaces were incubated overnight at 4°C with cFN^{RGD}, cFN$^{\Delta RGD}$, FNIII7-10^{RGD}, FNIII7-10$^{\Delta RGD}$, or FNIII7-10^{RGE} (all 50 µg/ml in PBS). For SCFS, we mounted a Nanowizard II atomic force microscope (AFM) equipped with a CellHesion module (both from JPK Instruments; Puech et al., 2006) onto an inverted fluorescence microscope (Observer Z1; Zeiss). The temperature was kept at 37°C throughout the experiment by a PetriDish heater (JPK Instruments). 200-µm-long V-shaped silicon nitride tip-less cantilevers having nominal spring constants of 0.06 N/m (NP-0; Bruker) were used. Each cantilever was calibrated prior the measurement by determining its sensitivity and spring constant using the thermal noise analysis of in-build routines (Hutter and Bechhoefer, 1993). To adhere a single fibroblast to the AFM cantilever, overnight serum-starved fibroblasts with confluency up to ~80% were washed with PBS, detached with 0.25% (wt/vol) trypsin/EDTA for 2 min, suspended in SCFS media (DMEM supplemented with 20 mM Hepes) containing 1% (vol/vol) FCS, pelleted, and finally resuspended in serum-free SCFS media. Fibroblasts were allowed to recover for at least 30 min from trypsin treatment (Schubert et al., 2014). Attachment of a single fibroblast to the free end of the cantilever was achieved by pipetting the fibroblast suspension onto functionalized Petri dishes. The functionalized cantilever was lowered onto a single fibroblast with a speed of 10 µm/s until a force of 5 nN was recorded. After 5 s contact, the cantilever was retracted at 10 µm/s for 100 µm, and the cantilever-bound fibroblast was incubated for 10–15 min for binding probability experiments and 7–10 min for adhesion force measurements to assure firm binding to the cantilever. Using differential interference contract microscopy, the morphological state of the fibroblast was monitored. For binding probability experiments, the fibroblast bound to the cantilever was lowered onto the coated substrate with a speed of 1 µm/s until a contact force of 200 pN, and the cantilever was

immediately, or after a contact time of 250 ms, retracted at 1 µm/s for ≥13 µm until the fibroblast and substrate were fully separated. This resulted in a total contact time between fibroblasts and substrate of ~50 ms or ~300 ms, respectively. After the experimental cycle, the fibroblast was allowed to recover for 0.5 s, and the contact area on the substrate was altered. This experimental cycle was repeated 100–200 times for each fibroblast used. FD curves were analyzed for unbinding events using in-build JPK software to determine binding probability as the ratio of FD curves showing unbinding events and total number of attempts. For adhesion force experiments, the rounded fibroblast bound to the cantilever was lowered onto the coated substrate with a speed of 5 µm/s until a contact force of 2 nN was recorded. For contact times of 5, 20, 50, or 120 s, the cantilever height was maintained constant. Subsequently, the cantilever was retracted at 5 µm/s and for 100 µm until the fibroblast and substrate were fully separated. After the experimental cycle, the fibroblast was allowed to recover for a time period equal to contact time before measuring the adhesion force for a different contact time. A single fibroblast was used to probe the adhesion force for all contact times or until morphological changes (that is, spreading) was observed. The sequence of contact time measurements and area of the substrate were varied. The adhesion of at least 10 fibroblasts was measured per condition to obtain statistically firm results. Adhesion forces were determined after baseline correction of FD curves with JPK software (JPK Instruments). Single unbinding forces were determined using an in-house-written Igor code (Igor 6; WaveMetrics). Two-tailed Mann-Whitney tests were applied to determine significant differences between the binding probability of fibroblast lines at different conditions. Mann-Whitney tests and statistical analysis of slope differences for linear fits were done using Prism (GraphPad) in-build routines.

Transgenic mouse strains

To generate the *Fn1*$^{\Delta RGD/\Delta RGD}$ mouse strain, part of the mouse FN gene was isolated from a phage library and subcloned, and the RGD sequence CGTGGGGAC, encoded by exon 30, was deleted by site-directed mutagenesis to generate the targeting vector (Fig. S2) for establishing mutant ES cells and finally *Fn1*$^{\Delta RGD/\Delta RGD}$ mice. The targeting vector contained a floxed neo cassette, which was removed by breeding the *Fn1*$^{\Delta RGD/\Delta RGD}$ mouse strain with a delete-Cre line. Mice and embryos were genotyped by Southern blot and genomic PCR (see Fig. S2) with DNA from tail or yolk sac biopsies using the primers 5′-CAAAGAAGACCCCAAGAG CA-3′ (forward) and 5′-ACAAGCCCTGGCCTTTAGTT-3′ (reverse). The *Fn1*$^{RGE/RGE}$ strain was previously established and genotyped as described previously (Takahashi et al., 2007). Time mattings were performed to recover E7.5, E8.5, and E9.5 embryos.

Fn1$^{flox/+}$ mice (Sakai et al., 2001) were mated with Cre-deleter line to generate *Fn1*$^{-/+}$ mice, which were subsequently intercrossed to generate *Fn1*$^{-/-}$ embryos.

Histology

Embryos were isolated and fixed in 4% phosphate-buffered PFA, embedded in tissue freezing medium (Leica), and sectioned at 7-µm thickness. Sections were immunostained and imaged with

a Zeiss fluorescence microscope equipped with an Axiocam MRm (monochrome charge-coupled device) using AxioVision software and a Zeiss confocal LSM 780.

Cell lines

To establish $Fn1^{\Delta RGD/\Delta RGD}$ and $Fn1^{+/+}$ fibroblast cell lines, blastocysts were flushed from the oviduct of heterozygous $Fn1^{+/\Delta RGD}$ intercrosses at E3.5 and cultured in DMEM containing 20% FCS (Thermo Fisher Scientific), 1,000 U/ml leukemia inhibitory factor, and 7×10^{-4} β-mercaptoethanol to generate ES cells as described previously (Fässler et al., 1995). To differentiate ES cells into fibroblasts, medium was changed to DMEM supplemented with 10% FCS and 1% DMSO. Finally, the fibroblasts were immortalized by retroviral transduction of the SV-40 large T antigen and cloned.

$Fn1$-null fibroblasts, $Fn1^{RGE/RGE}$ fibroblasts, and pKO, pKO-β1, pKO-αv, and pKO-β1/αv integrin–expressing fibroblasts have previously been described and characterized (Schiller et al., 2013; Takahashi et al., 2007; Sakai et al., 2001). All fibroblast cell lines were grown in DMEM containing 10% FCS and 1% penicillin-streptomycin (Gibco).

Quantitative real-time PCR

RNA was isolated using RNeasy Kit (Qiagen). The sequences of the oligonucleotides used were 5′-TCCAAATCAGAAGCTCCAA CAA-3′ for *Itga8* forward, 5′-CGCTCACGAAATTGCTGTCA-3′ for *Itga8* reverse, 5′-ACCCAGAAGACTGTGGATGG-3′ for *GAPDH* forward, and 5′-ACACATTGGGGGTAGGAACA-3′ for *GAPDH* reverse.

Surface integrin analysis by flow cytometry

Cells were detached with trypsin, and trypsinization was stopped with 100 μg/ml trypsin inhibitor (Calbiochem). Cells were washed with PBS and finally resuspended in FACS buffer (3% BSA in TBS). Cells were counted, and ~5 × 10^5 cells were distributed in round-bottom wells of 96-well plates or in a round-bottom polystyrene tube, spun down, and resuspended in primary antibody or isotype control dilution (1:200) in FACS buffer. Cells were stained for 30 min on ice followed by two cycles of centrifugation and resuspension in FACS buffer to wash out the unbound antibody. When nonlabeled antibodies were used, an extra incubation step with labeled secondary antibody diluted 1:200 in FACS buffer was done (30 min on ice), followed by two cycles of washes. Stained cells were then resuspended in 300 μl FACS buffer and analyzed in a FACSCanto (BD Bioscience). During analysis, the same settings of forward scatter and side scatter were used to select size and granularity for each cell line, which were established using and nonlabeled sample of each cell line. These settings were maintained among replicates and experiments. Also, for comparison of different cell lines, the same laser and detector settings were used. Data were evaluated using FlowJo (BD Bioscience), and fluorescence intensity measurements were normalized using the intensity values of the isotype control for each antibody. Experiments were done three times with technical triplicates in each experiment.

FN purification

To purify cFN, wild-type and mutant fibroblast cells were grown to 100% confluence in DMEM containing 10% FCS. The medium

was removed, and cells were washed three times with SRM 46.5% AIM-V (Life Technologies), 5% RPMI (Life Technologies), and 1% non-essential amino acid solution (Sigma-Aldrich) and left overnight. The SRM was discarded, replaced by fresh SRM, and collected every alternative day. cFN$^{\Delta RGD}$, cFN^{RGE}, and cFN^{RGD} were purified from the conditioned SRMs using gelatin-Sepharose columns as described previously (Akiyama, 2013). Briefly, media were centrifuged to pellet down cell debris. Media were incubated with gelatin-Sepharose (GE Healthcare Life Sciences), columns were washed with TBS (0.15 M NaCl in 10 mM Tris-HCl, pH 7.4), and cFN was eluted with 4 M urea in TBS and dialyzed against TBS. Purified FN was analyzed by 8% SDS-PAGE and stained with Coomassie brilliant blue and by WB.

Antibodies and F-actin labels

For flow cytometry, the following antibodies conjugated to PE were used: hamster anti-mouse β1 integrin (1:200; 102207; BioLegend), rat anti-mouse α5 integrin (1:200; 557447; PharMingen), hamster anti-mouse β3 integrin (1:200; 12–0611; BD Biosciences), rat anti-mouse αv integrin (1:200; 551187; PharMingen), rat anti-mouse α4 integrin (1:200; 01271D; PharMingen), and unconjugated rat anti-mouse syndecan 4 (1:200; 550350; PharMingen) together with mouse anti-rat FITC (10094D; PharMingen).

The following primary antibodies were used for immunostaining (IF) and WB: rabbit anti-FN (1:600 for IF and 1:5,000 for WB; AB2033; Millipore), rabbit anti-Nidogen (1:1,500; generous gift from Dr. Rupert Timpl, Max Planck Institute of Biochemistry, Martinsried, Germany), mouse monoclonal anti-paxillin (1:300; 610051; BD Transduction Laboratories), rat anti-tubulin (1:3,000; MAB1318; Millipore), mouse monoclonal anti-mouse syndecan 1 (1:2,000; sc-12765; Santa Cruz Biotechnology); mouse monoclonal anti-mouse syndecan 2 (1:2,000; sc-376160; Santa Cruz Biotechnology); mouse monoclonal anti-mouse syndecan 3 (1:2,000; sc-398194; Santa Cruz Biotechnology); and mouse monoclonal anti-mouse syndecan 4 (1:2,000; sc-12766; Santa Cruz Biotechnology).

The secondary antibodies used for IF were: goat anti-rabbit conjugated with Cy3 (1:5,000; ab6939; Abcam), goat anti-rabbit conjugated with Alexa488 (1:500; A11008; Molecular Probes), donkey anti-mouse conjugated with Alexa647 (1:500; A31571; Molecular Probes), goat anti-rabbit Alexa647 (1:500; ab150083; Abcam), goat anti-mouse Alexa488 (1:500; A32723; Molecular Probes). The secondary antibodies used for WB were all diluted 1:1,000: goat anti-rabbit conjugated with horseradish peroxidase (172-1019; Bio-Rad), goat anti-mouse conjugated with horseradish peroxidase (170-6516; Bio-Rad) and goat anti-rat conjugated with horseradish peroxidase (5204-2504; Bio-Rad).

To label actin filaments, we used phalloidin labeled with either tetramethylrhodamine B isothiocyanate (1:500; P1951; Sigma-Aldrich) or fluorescein isothiocyanate (1:500; P5282; Sigma-Aldrich).

Adhesion assays to cFN

Glass coverslips of 18 × 18 mm were poly-maleic anhydride-1-octadecene treated (Prewitz et al., 2013), coated with 20 μg/ml purified mouse cFN for 1 h at 37°C, blocked for 30 min at RT with

3% BSA in PBS, and then seeded with 3×10^4 fibroblasts starved overnight in SRM, detached with 2 mM EDTA in PBS, and resuspended in DMEM. After 90 min of culture in DMEM, cells were fixed 10 min with 4% PFA, washed with PBS, permeabilized with 0.1% Triton X-100, and processed for IF. Images were taken at 22°C with a confocal Olympus FV1000 microscope with 40× (NA 1.30 oil) and 63× (NA 1.35 oil) objectives using the 488-, 594-, and 635-nm laser lines for fluorochrome detection. Spreading areas were calculated using the polygonal selection tool of ImageJ. Between 20 and 30 cells from three independent experiments were analyzed.

FN fibrillogenesis assay

$Fn1^{\Delta RGD/\Delta RGD}$ and $Fn1^{+/+}$ ES cells were induced to grow in DMEM high glucose supplemented with 6% FCS (FN depleted), 1.4% methylcellulose, 450 µM monothioglycerol (Sigma-Aldrich), and 10 µg/ml human insulin (Sigma-Aldrich). Approximately 2.5×10^3 ES cells in 2 ml medium were seeded in a 35-mm dish and grown for 11 d without changing the medium, allowing formation of cell aggregates and assembly of their own secreted FN. Afterward, the ES cell aggregates were centrifuged and included into 15% gelatin to form a block. The gelatinized block was fixed with 4% PFA at 4°C for 1 h, washed with PBS, and cryoprotected with 7.5% (3 h) and 15% (overnight) sucrose. Blocks were embedded in tissue freezing medium (Leica) for cryosectioning and IF.

For FN assembly with $Fn1^{+/+}$, $Fn1^{\Delta RGD/\Delta RGD}$, and $Fn1^{RGE/RGE}$ fibroblasts, cells were prestarved overnight with SRM containing 1% FN-depleted calf serum and detached with 2 mM EDTA, and 15×10^3 cells were seeded onto glass coverslips coated with 10 µg/ml laminin (from Engelbreth-Holm-Swarm murine sarcoma BM; L2020; Sigma-Aldrich), VN (07180; Stem Cell), or collagen type I (PureCol, 5005; Advanced BioMatrix) for 1 h at RT and blocked for 1 h with 1% BSA-PBS. Cells were cultured for indicated times in SRM. Cells were then fixed with 4% paraformaldehyde and immunostained.

To block the FN heparin-binding sites, cells were seeded for 3 h in SRM, which was then replaced by SRM containing 0.1 mg/ml heparin (Sigma-Aldrich) for 24 or 72 h. $MnCl_2$ was added to the cell culture medium for 3 h at a concentration of 100 µM. Slides were then mounted with Elvanol No-Fade mounting medium. Images were taken at 22°C with a Zeiss confocal LSM 780 microscope using a 100× (NA 1.46 oil) objective and ZEN2010 software for acquisition. For detection of Alexa Fluor, the 488-, 561-, and 633-nm laser lines were used. Images were processed, merged, and gamma adjusted in Fiji ImageJ (version 1.37).

Image analysis of fibrillar FN

Pictures were processed, analyzed, and merged in Fiji ImageJ. To measure the FN network in Fig. S5 a, the area of extracellular FN stained was quantified and normalized to the total area of each image and cell numbers. The amount of FN branches was quantified as described in Zhang et al. (2020). Briefly, pictures were set to binary 8 bits, the same threshold was set for all of them, noise was removed with a despeckle function and Skeleton plugin, and analysis was applied by Fiji ImageJ. The amount of FN branches was summarized and normalized to the total number of cells and image area.

DOC extraction of cell lysates

To differentiate between cell-soluble FN and FN assembled into an insoluble network, $\sim 5 \times 10^3$ cells were seeded on laminin (10 µg/ml)-coated 24-well plates and starved overnight with SRM. For heparin-treated cells, SRM was replaced after 3 h with SRM containing 0.1 mg/ml heparin. Cells and medium were collected after 24, 72, and 120 h of incubation and processed for WB. To this end, cells were washed with PBS twice, lysed with DOC buffer (2% DOC, 2 mM Tris-HCl, pH 8.8, and 2 mM EDTA) containing protease inhibitors (cOmplete; 05892970001; Roche) for 10 min on ice and then passed through a 25-gauge syringe and centrifuged at 14,000 rpm for 20 min. The clear supernatant was collected and kept as the soluble FN fraction (intracellular), while the pellet was washed with DOC buffer and centrifuged again to obtain the final pellet containing the cross-linked (fibrillar) FN network, which was resuspended in 1% SDS, 2 mM Tris-HCl, pH 8.8, and 2 mM EDTA containing protease inhibitors. Half of the DOC-soluble and the whole insoluble fractions were separated in an 8% SDS gel. The culture medium was centrifugated to pellet cell debris and directly loaded in the SDS gel to determine the soluble FN remaining in the culture medium. Proteins were transferred onto a polyvinylidene difluoride membrane and processed with antibodies. FN levels were measured using Fiji ImageJ and normalized to tubulin levels present in the cellular fraction.

Syndecan 1–4 knockdown

Syndecan mRNA translation was blocked in $Fn1^{\Delta RGD/\Delta RGD}$ cells by gene silencing with siRNA. 150 nM of predesigned siRNA pools (SMARTpool; Dharmacon) against syndecan 1 (Sdc1; reference no. 20969) and syndecan 4 (Sdc4; reference no. 20971) were lipofected into subconfluent, overnight-starved fibroblasts (Lipofectamine 3000; Invitrogen) seeded on laminin-coated coverslips in SRM during a 3-h period before transfection. The SRM was replaced 12 h after transfection, and cells were incubated for 96 h in SRM and then processed for IF. Syndecan levels were analyzed by WB to check gene silencing and compare with cells transfected with siRNAs containing an scr sequence.

Statistical analysis

In Fig. 1, Fig. S1, and Table S1, two-tailed Mann-Whitney tests were performed to test for significance using Prism (GraphPad). The n (number of cells or analyzed FD curves) and P values are indicated in the figure. In Figs. 2, 3, 4, and 5 and corresponding supplementary figures, data are presented as means ± SD of the mean (SEM). Each experiment was independently performed at least three times. The sample number (n) used for statistical testing is indicated in the corresponding figure legend. P values are indicated in each figure (*, P < 0.05; **, P < 0.01; and ***, P < 0.001). All P values are from two-tailed unpaired t tests, and Bonferroni correction was performed for tests with multiple pairwise comparisons. Statistical analysis was performed using Prism (GraphPad Software). Data distribution was assumed to be normal, but this was not formally tested.

Online supplemental material

Fig. S1 shows the AFM-based SCFS setup that we used to quantify adhesion of fibroblasts to different full-length cFNs and FNIII7-10 fragments. It also shows the relative frequency distribution of unbinding events in experiments with a contact time of ~300 ms and the adhesion strengthening dynamics for each condition. Fig. S2 illustrates the strategy to generate $Fn1^{\Delta RGD/\Delta RGD}$ mice and their histological analysis by immunofluorescence to different ECM proteins (FN, laminin, and collagen type IV). Fig. S3 shows surface β1, β3, α5, αv, and α4 integrins and syndecan 4 levels and $Itga8$ expression in the different cell lines. Fig. S4 presents FN^{RGD} and FN$^{\Delta RGD}$ assembly by cells cultured on VN- or collagen I–coated glass. Fig. S5 shows FN^{RGD}, FN^{RGE}, and FN$^{\Delta RGD}$ assembly and quantification in the presence of heparin and/or Mn^{+2}. It also shows the levels of syndecans in Fn1$^{\Delta RGD/\Delta RGD}$ and Fn1+/+ cells after knockdown with siRNAs and the quantification of FN fibrils assembled by the cells on each condition. Table S1 displays the statistical comparison of adhesion-strengthening dynamics of pKO-αv, pKO-β1, pKO-αv/β1, and pKO cell lines to FNIII7-10$^{\Delta RGD}$, FNIII7-10^{RGD}, or FNIII7-10^{RGE} fragments.

Acknowledgments

References

Akiyama, S.K. 2013. Purification of fibronectin. *Curr. Protoc. Cell Biol.* 60:Unit 10.5. https://doi.org/10.1002/0471143030.cb1005s60

Bader, B.L., H. Rayburn, D. Crowley, and R.O. Hynes. 1998. Extensive vasculogenesis, angiogenesis, and organogenesis precede lethality in mice lacking all alpha v integrins. *Cell.* 95:507–519. https://doi.org/10.1016/S0092-8674(00)81618-9

Bass, M.D., K.A. Roach, M.R. Morgan, Z. Mostafavi-Pour, T. Schoen, T. Muramatsu, U. Mayer, C. Ballestrem, J.P. Spatz, and M.J. Humphries. 2007. Syndecan-4-dependent Rac1 regulation determines directional

migration in response to the extracellular matrix. *J. Cell Biol.* 177: 527–538. https://doi.org/10.1083/jcb.200610076

Bass, M.D., R.C. Williamson, R.D. Nunan, J.D. Humphries, A. Byron, M.R. Morgan, P. Martin, and M.J. Humphries. 2011. A syndecan-4 hair trigger initiates wound healing through caveolin- and RhoG-regulated integrin endocytosis. *Dev. Cell.* 21:681–693. https://doi.org/10.1016/j.devcel.2011.08.007

Beauvais, D.M., and A.C. Rapraeger. 2010. Syndecan-1 couples the insulinlike growth factor-1 receptor to inside-out integrin activation. *J. Cell Sci.* 123:3796–3807. https://doi.org/10.1242/jcs.067645

Benito-Jardón, M., S. Klapproth, I. Gimeno-LLuch, T. Petzold, M. Bharadwaj, D.J. Müller, G. Zuchtriegel, C.A. Reichel, and M. Costell. 2017. The fibronectin synergy site re-enforces cell adhesion and mediates a crosstalk between integrin classes. *eLife.* 6:e22264. https://doi.org/10.7554/eLife.22264

Beumer, S., G.J. Heijnen-Snyder, M.J. IJsseldijk, P.G. de Groot, and J.J. Sixma. 2000. Fibronectin in an extracellular matrix of cultured endothelial cells supports platelet adhesion via its ninth type III repeat : A comparison with platelet adhesion to isolated fibronectin. *Arterioscler. Thromb. Vasc. Biol.* 20:E16–E25. https://doi.org/10.1161/01.ATV.20.4.e16

Bharadwaj, M., N. Strohmeyer, G.P. Colo, J. Helenius, N. Beerenwinkel, H.B. Schiller, R. Fässler, and D.J. Müller. 2017. αV-class integrins exert dual roles on α5β1 integrins to strengthen adhesion to fibronectin. *Nat. Commun.* 8:14348. https://doi.org/10.1038/ncomms14348

Bloom, L., K.C. Ingham, and R.O. Hynes. 1999. Fibronectin regulates assembly of actin filaments and focal contacts in cultured cells via the heparin-binding site in repeat III13. *Mol. Biol. Cell.* 10:1521–1536. https://doi.org/10.1091/mbc.10.5.1521

Cherny, R.C., M.A. Honan, and P. Thiagarajan. 1993. Site-directed mutagenesis of the arginine-glycine-aspartic acid in vitronectin abolishes cell adhesion. *J. Biol. Chem.* 268:9725–9729.

Chronopoulos, A., S.D. Thorpe, E. Cortes, D. Lachowski, A.J. Rice, V.V. Mykuliak, T. Róg, D.A. Lee, V.P. Hytönen, and A.E. Del Río Hernández. 2020. Syndecan-4 tunes cell mechanics by activating the kindlin-integrin-RhoA pathway. *Nat. Mater.* 19:669–678. https://doi.org/10.1038/s41563-019-0567-1

Chung, C.Y., and H.P. Erickson. 1997. Glycosaminoglycans modulate fibronectin matrix assembly and are essential for matrix incorporation of tenascin-C. *J. Cell Sci.* 110:1413–1419.

Curnis, F., R. Longhi, L. Crippa, A. Cattaneo, E. Dondossola, A. Bachi, and A. Corti. 2006. Spontaneous formation of L-isoaspartate and gain of function in fibronectin. *J. Biol. Chem.* 281:36466–36476. https://doi.org/10.1074/jbc.M604812200

Curnis, F., A. Cattaneo, R. Longhi, A. Sacchi, A.M. Gasparri, F. Pastorino, P. Di Matteo, C. Traversari, A. Bachi, M. Ponzoni, et al. 2010. Critical role of flanking residues in NGR-to-isoDGR transition and CD13/integrin receptor switching. *J. Biol. Chem.* 285:9114–9123. https://doi.org/10.1074/jbc.M109.044297

Dallas, S.L., P. Sivakumar, C.J.P. Jones, Q. Chen, D.M. Peters, D.F. Mosher, M.J. Humphries, and C.M. Kielty. 2005. Fibronectin regulates latent transforming growth factor-beta (TGF beta) by controlling matrix assembly of latent TGF beta-binding protein-1. *J. Biol. Chem.* 280:18871–18880. https://doi.org/10.1074/jbc.M410762200

Erdogan, B., M. Ao, L.M. White, A.L. Means, B.M. Brewer, L. Yang, M.K. Washington, C. Shi, O.E. Franco, A.M. Weaver, et al. 2017. Cancer-associated fibroblasts promote directional cancer cell migration by aligning fibronectin. *J. Cell Biol.* 216:3799–3816. https://doi.org/10.1083/jcb.201704053

Fässler, R., M. Pfaff, J. Murphy, A.A. Noegel, S. Johansson, R. Timpl, and R. Albrecht. 1995. Lack of beta 1 integrin gene in embryonic stem cells affects morphology, adhesion, and migration but not integration into the inner cell mass of blastocysts. *J. Cell Biol.* 128:979–988. https://doi.org/10.1083/jcb.128.5.979

Friedrichs, J., K.R. Legate, R. Schubert, M. Bharadwaj, C. Werner, D.J. Müller, and M. Benoit. 2013. A practical guide to quantify cell adhesion using single-cell force spectroscopy. *Methods.* 60:169–178. https://doi.org/10.1016/j.ymeth.2013.01.006

Galante, L.L., and J.E. Schwarzbauer. 2007. Requirements for sulfate transport and the diastrophic dysplasia sulfate transporter in fibronectin matrix assembly. *J. Cell Biol.* 179:999–1009. https://doi.org/10.1083/jcb.200707150

George, E.L., E.N. Georges-Labouesse, R.S. Patel-King, H. Rayburn, and R.O. Hynes. 1993. Defects in mesoderm, neural tube and vascular development in mouse embryos lacking fibronectin. *Development.* 119: 1079–1091.

Georges-Labouesse, E.N., E.L. George, H. Rayburn, and R.O. Hynes. 1996. Mesodermal development in mouse embryos mutant for fibronectin. *Dev. Dyn.* 207:145–156. https://doi.org/10.1002/(SICI)1097-0177(199610)207:2<145::AID-AJA3>3.0.CO;2-H

Girós, A., K. Grgur, A. Gossler, and M. Costell. 2011. α5β1 integrin-mediated adhesion to fibronectin is required for axis elongation and somitogenesis in mice. *PLoS One.* 6:e22002. https://doi.org/10.1371/journal.pone.0022002

Greenspoon, N., R. Hershkoviz, R. Alon, D. Varon, B. Shenkman, G. Marx, S. Federman, G. Kapustina, and O. Lider. 1993. Structural analysis of integrin recognition and the inhibition of integrin-mediated cell functions by novel nonpeptidic surrogates of the Arg-Gly-Asp sequence. *Biochemistry.* 32:1001–1008. https://doi.org/10.1021/bi00055a002

Hutter, J.L., and J. Bechhoefer. 1993. Calibration of atomic-force microscope tips. *Rev. Sci. Instrum.* 64:1868–1873. https://doi.org/10.1063/1.1143970

Kadler, K.E., A. Hill, and E.G. Canty-Laird. 2008. Collagen fibrillogenesis: fibronectin, integrins, and minor collagens as organizers and nucleators. *Curr. Opin. Cell Biol.* 20:495–501. https://doi.org/10.1016/j.ceb.2008.06.008

Klass, C.M., J.R. Couchman, and A. Woods. 2000. Control of extracellular matrix assembly by syndecan-2 proteoglycan. *J. Cell Sci.* 113:493–506.

Korntner, S., C. Lehner, R. Gehwolf, A. Wagner, M. Grütz, N. Kunkel, H. Tempfer, and A. Traweger. 2019. Limiting angiogenesis to modulate scar formation. *Adv. Drug Deliv. Rev.* 146:170–189. https://doi.org/10.1016/j.addr.2018.02.010

Kozlova, N.I., G.E. Morozevich, A.N. Chubukina, and A.E. Berman. 2001. Integrin alphavbeta3 promotes anchorage-dependent apoptosis in human intestinal carcinoma cells. *Oncogene.* 20:4710–4717. https://doi.org/10.1038/sj.onc.1204619

Lee, J., B. Park, B. Moon, J. Park, H. Moon, K. Kim, S.-A. Lee, D. Kim, C. Min, D.-H. Lee, et al. 2019. A scaffold for signaling of Tim-4-mediated efferocytosis is formed by fibronectin. *Cell Death Differ.* 26:1646–1655. https://doi.org/10.1038/s41418-018-0238-9

Leiss, M., K. Beckmann, A. Girós, M. Costell, and R. Fässler. 2008. The role of integrin binding sites in fibronectin matrix assembly in vivo. *Curr. Opin. Cell Biol.* 20:502–507. https://doi.org/10.1016/j.ceb.2008.06.001

Leyton, L., P. Schneider, C.V. Labra, C. Rüegg, C.A. Hetz, A.F. Quest, and C. Bron. 2001. Thy-1 binds to integrin beta(3) on astrocytes and triggers formation of focal contact sites. *Curr. Biol.* 11:1028–1038. https://doi.org/10.1016/S0960-9822(01)00262-7

Lovett, M., K. Lee, A. Edwards, and D.L. Kaplan. 2009. Vascularization strategies for tissue engineering. *Tissue Eng. Part B Rev.* 15:353–370. https://doi.org/10.1089/ten.teb.2009.0085

Lu, J., A.D. Doyle, Y. Shinsato, S. Wang, M.A. Bodendorfer, M. Zheng, and K.M. Yamada. 2020. Basement Membrane Regulates Fibronectin Organization Using Sliding Focal Adhesions Driven by a Contractile Winch. *Dev. Cell.* 52:631–646.e4. https://doi.org/10.1016/j.devcel.2020.01.007

Mahalingam, Y., J.T. Gallagher, and J.R. Couchman. 2007. Cellular adhesion responses to the heparin-binding (HepII) domain of fibronectin require heparan sulfate with specific properties. *J. Biol. Chem.* 282:3221–3230. https://doi.org/10.1074/jbc.M604938200

Mamidi, A., C. Prawiro, P.A. Seymour, K.H. de Lichtenberg, A. Jackson, P. Serup, and H. Semb. 2018. Mechanosignalling via integrins directs fate decisions of pancreatic progenitors. *Nature.* 564:114–118. https://doi.org/10.1038/s41586-018-0762-2

Mao, Y., and J.E. Schwarzbauer. 2005. Fibronectin fibrillogenesis, a cell-mediated matrix assembly process. *Matrix Biol.* 24:389–399. https://doi.org/10.1016/j.matbio.2005.06.008

Marín-Pareja, N., M. Cantini, C. González-García, E. Salvagni, M. Salmerón-Sánchez, and M.-P. Ginebra. 2015. Different Organization of Type I Collagen Immobilized on Silanized and Nonsilanized Titanium Surfaces Affects Fibroblast Adhesion and Fibronectin Secretion. *ACS Appl. Mater. Interfaces.* 7:20667–20677. https://doi.org/10.1021/acsami.5b05420

McDonald, J.A. 1988. Extracellular matrix assembly. *Annu. Rev. Cell Biol.* 4:183–207. https://doi.org/10.1146/annurev.cb.04.110188.001151

Morgan, M.R., M.J. Humphries, and M.D. Bass. 2007. Synergistic control of cell adhesion by integrins and syndecans. *Nat. Rev. Mol. Cell Biol.* 8:957–969. https://doi.org/10.1038/nrm2289

Nakamura, I., L.T. Duong, S.B. Rodan, and G.A. Rodan. 2007. Involvement of alpha(v)beta3 integrins in osteoclast function. *J. Bone Miner. Metab.* 25:337–344. https://doi.org/10.1007/s00774-007-0773-9

Niederlechner, S., J. Klawitter, C. Baird, A.R. Kallweit, U. Christians, and P.E. Wischmeyer. 2012. Fibronectin-integrin signaling is required for L-glutamine's protection against gut injury. *PLoS One.* 7:e50185. https://doi.org/10.1371/journal.pone.0050185

Pankov, R., E. Cukierman, B.Z. Katz, K. Matsumoto, D.C. Lin, S. Lin, C. Hahn, and K.M. Yamada. 2000. Integrin dynamics and matrix assembly: tensin-dependent translocation of alpha(5)beta(1) integrins promotes early fibronectin fibrillogenesis. *J. Cell Biol.* 148:1075–1090. https://doi.org/10.1083/jcb.148.5.1075

Peterson, J.A., N. Sheibani, G. David, A. Garcia-Pardo, and D.M. Peters. 2005. Heparin II domain of fibronectin uses alpha4beta1 integrin to control focal adhesion and stress fiber formation, independent of syndecan-4. *J. Biol. Chem.* 280:6915–6922. https://doi.org/10.1074/jbc.M406625200

Prewitz, M.C., F.P. Seib, M. von Bonin, J. Friedrichs, A. Stißel, C. Niehage, K. Müller, K. Anastassiadis, C. Waskow, B. Hoflack, et al. 2013. Tightly anchored tissue-mimetic matrices as instructive stem cell microenvironments. *Nat. Methods.* 10:788–794. https://doi.org/10.1038/nmeth.2523

Puech, P.-H., K. Poole, D. Knebel, and D.J. Müller. 2006. A new technical approach to quantify cell-cell adhesion forces by AFM. *Ultramicroscopy.* 106:637–644. https://doi.org/10.1016/j.ultramic.2005.08.003

Roper, J.A., R.C. Williamson, and M.D. Bass. 2012. Syndecan and integrin interactomes: large complexes in small spaces. *Curr. Opin. Struct. Biol.* 22:583–590. https://doi.org/10.1016/j.sbi.2012.07.003

Ruoslahti, E., and M.D. Pierschbacher. 1987. New perspectives in cell adhesion: RGD and integrins. *Science.* 238:491–497. https://doi.org/10.1126/science.2821619

Sakai, T., K.J. Johnson, M. Murozono, K. Sakai, M.A. Magnuson, T. Wieloch, T. Cronberg, A. Isshiki, H.P. Erickson, and R. Fässler. 2001. Plasma fibronectin supports neuronal survival and reduces brain injury following transient focal cerebral ischemia but is not essential for skin-wound healing and hemostasis. *Nat. Med.* 7:324–330. https://doi.org/10.1038/85471

Salmerón-Sánchez, M., P. Rico, D. Moratal, T.T. Lee, J.E. Schwarzbauer, and A.J. García. 2011. Role of material-driven fibronectin fibrillogenesis in cell differentiation. *Biomaterials.* 32:2099–2105. https://doi.org/10.1016/j.biomaterials.2010.11.057

Schiller, H.B., M.-R. Hermann, J. Polleux, T. Vignaud, S. Zanivan, C.C. Friedel, Z. Sun, A. Raducanu, K.-E. Gottschalk, M. Théry, et al. 2013. β1- and αv-class integrins cooperate to regulate myosin II during rigidity sensing of fibronectin-based microenvironments. *Nat. Cell Biol.* 15:625–636. https://doi.org/10.1038/ncb2747

Schubert, R., N. Strohmeyer, M. Bharadwaj, S.P. Ramanathan, M. Krieg, J. Friedrichs, C.M. Franz, and D.J. Müller. 2014. Assay for characterizing the recovery of vertebrate cells for adhesion measurements by single-cell force spectroscopy. *FEBS Lett.* 588:3639–3648. https://doi.org/10.1016/j.febslet.2014.06.012

Sechler, J.L., A.M. Cumiskey, D.M. Gazzola, and J.E. Schwarzbauer. 2000. A novel RGD-independent fibronectin assembly pathway initiated by alpha4beta1 integrin binding to the alternatively spliced V region. *J. Cell Sci.* 113:1491–1498.

Shiokawa, S., Y. Yoshimura, H. Sawa, S. Nagamatsu, H. Hanashi, K. Sakai, M. Ando, and Y. Nakamura. 1999. Functional role of arg-gly-asp (RGD)-binding sites on beta1 integrin in embryo implantation using mouse blastocysts and human decidua. *Biol. Reprod.* 60:1468–1474. https://doi.org/10.1095/biolreprod60.6.1468

Singh, P., C. Carraher, and J.E. Schwarzbauer. 2010. Assembly of fibronectin extracellular matrix. *Annu. Rev. Cell Dev. Biol.* 26:397–419. https://doi.org/10.1146/annurev-cellbio-100109-104020

Sottile, J., and D.C. Hocking. 2002. Fibronectin polymerization regulates the composition and stability of extracellular matrix fibrils and cell-matrix adhesions. *Mol. Biol. Cell.* 13:3546–3559. https://doi.org/10.1091/mbc.e02-01-0048

Spoerri, P.M., N. Strohmeyer, Z. Sun, R. Fässler, and D.J. Müller. 2020. Protease-activated receptor signalling initiates α5β1-integrin-mediated adhesion in non-haematopoietic cells. *Nat. Mater.* 19:218–226. https://doi.org/10.1038/s41563-019-0580-4

Stepp, M.A., W.P. Daley, A.M. Bernstein, S. Pal-Ghosh, G. Tadvalkar, A. Shashurin, S. Palsen, R.A. Jurjus, and M. Larsen. 2010. Syndecan-1 regulates cell migration and fibronectin fibril assembly. *Exp. Cell Res.* 316:2322–2339. https://doi.org/10.1016/j.yexcr.2010.05.020

Strohmeyer, N., M. Bharadwaj, M. Costell, R. Fässler, and D.J. Müller. 2017. Fibronectin-bound α5β1 integrins sense load and signal to reinforce adhesion in less than a second. *Nat. Mater.* 16:1262–1270. https://doi.org/10.1038/nmat5023

Takahashi, S., M. Leiss, M. Moser, T. Ohashi, T. Kitao, D. Heckmann, A. Pfeifer, H. Kessler, J. Takagi, H.P. Erickson, and R. Fässler. 2007. The RGD motif in fibronectin is essential for development but dispensable for fibril assembly. *J. Cell Biol.* 178:167–178. https://doi.org/10.1083/jcb.200703021

Twal, W.O., A. Czirók, B. Hegedus, C. Knaak, M.R. Chintalapudi, H. Okagawa, Y. Sugi, and W.S. Argraves. 2001. Fibulin-1 suppression of fibronectin-regulated cell adhesion and motility. *J. Cell Sci.* 114:4587–4598.

Wang, Z., R.J. Collighan, S.R. Gross, E.H.J. Danen, G. Orend, D. Telci, and M. Griffin. 2010. RGD-independent cell adhesion via a tissue transglutaminase-fibronectin matrix promotes fibronectin fibril deposition and requires syndecan-4/2 α5β1 integrin co-signaling. *J. Biol. Chem.* 285:40212–40229. https://doi.org/10.1074/jbc.M110.123703

Wennerberg, K., L. Lohikangas, D. Gullberg, M. Pfaff, S. Johansson, and R. Fässler. 1996. Beta 1 integrin-dependent and -independent polymerization of fibronectin. *J. Cell Biol.* 132:227–238. https://doi.org/10.1083/jcb.132.1.227

Wilson, C.J., R.E. Clegg, D.I. Leavesley, and M.J. Pearcy. 2005. Mediation of biomaterial-cell interactions by adsorbed proteins: a review. *Tissue Eng.* 11:1–18. https://doi.org/10.1089/ten.2005.11.1

Woods, A., and J.R. Couchman. 1994. Syndecan 4 heparan sulfate proteoglycan is a selectively enriched and widespread focal adhesion component. *Mol. Biol. Cell.* 5:183–192. https://doi.org/10.1091/mbc.5.2.183

Woods, A., R.L. Longley, S. Tumova, and J.R. Couchman. 2000. Syndecan-4 binding to the high affinity heparin-binding domain of fibronectin drives focal adhesion formation in fibroblasts. *Arch. Biochem. Biophys.* 374:66–72. https://doi.org/10.1006/abbi.1999.1607

Xu, J., L.M. Maurer, B.R. Hoffmann, D.S. Annis, and D.F. Mosher. 2010. iso-DGR sequences do not mediate binding of fibronectin N-terminal modules to adherent fibronectin-null fibroblasts. *J. Biol. Chem.* 285:8563–8571. https://doi.org/10.1074/jbc.M109.062646

Yang, N., and A. Friedl. 2016. Syndecan-1-Induced ECM Fiber Alignment Requires Integrin αvβ3 and Syndecan-1 Ectodomain and Heparan Sulfate Chains. *PLoS One.* 11:e0150132–e25. https://doi.org/10.1371/journal.pone.0150132

Yang, J.T., and R.O. Hynes. 1996. Fibronectin receptor functions in embryonic cells deficient in alpha 5 beta 1 integrin can be replaced by alpha V integrins. *Mol. Biol. Cell.* 7:1737–1748. https://doi.org/10.1091/mbc.7.11.1737

Yang, J.T., H. Rayburn, and R.O. Hynes. 1993. Embryonic mesodermal defects in alpha 5 integrin-deficient mice. *Development.* 119:1093–1105.

Yang, J.T., B.L. Bader, J.A. Kreidberg, M. Ullman-Culleré, J.E. Trevithick, and R.O. Hynes. 1999. Overlapping and independent functions of fibronectin receptor integrins in early mesodermal development. *Dev. Biol.* 215:264–277. https://doi.org/10.1006/dbio.1999.9451

Yu, M., N. Strohmeyer, J. Wang, D.J. Müller, and J. Helenius. 2015. Increasing throughput of AFM-based single cell adhesion measurements through multisubstrate surfaces. *Beilstein J. Nanotechnol.* 6:157–166. https://doi.org/10.3762/bjnano.6.15

Zhang, R.M., H. Kumra, and D.P. Reinhardt. 2020. Quantification of Extracellular Matrix Fiber Systems Related to ADAMTS Proteins. *Methods Mol. Biol.* 2043:237–250. https://doi.org/10.1007/978-1-4939-9698-8_19

Supplemental material
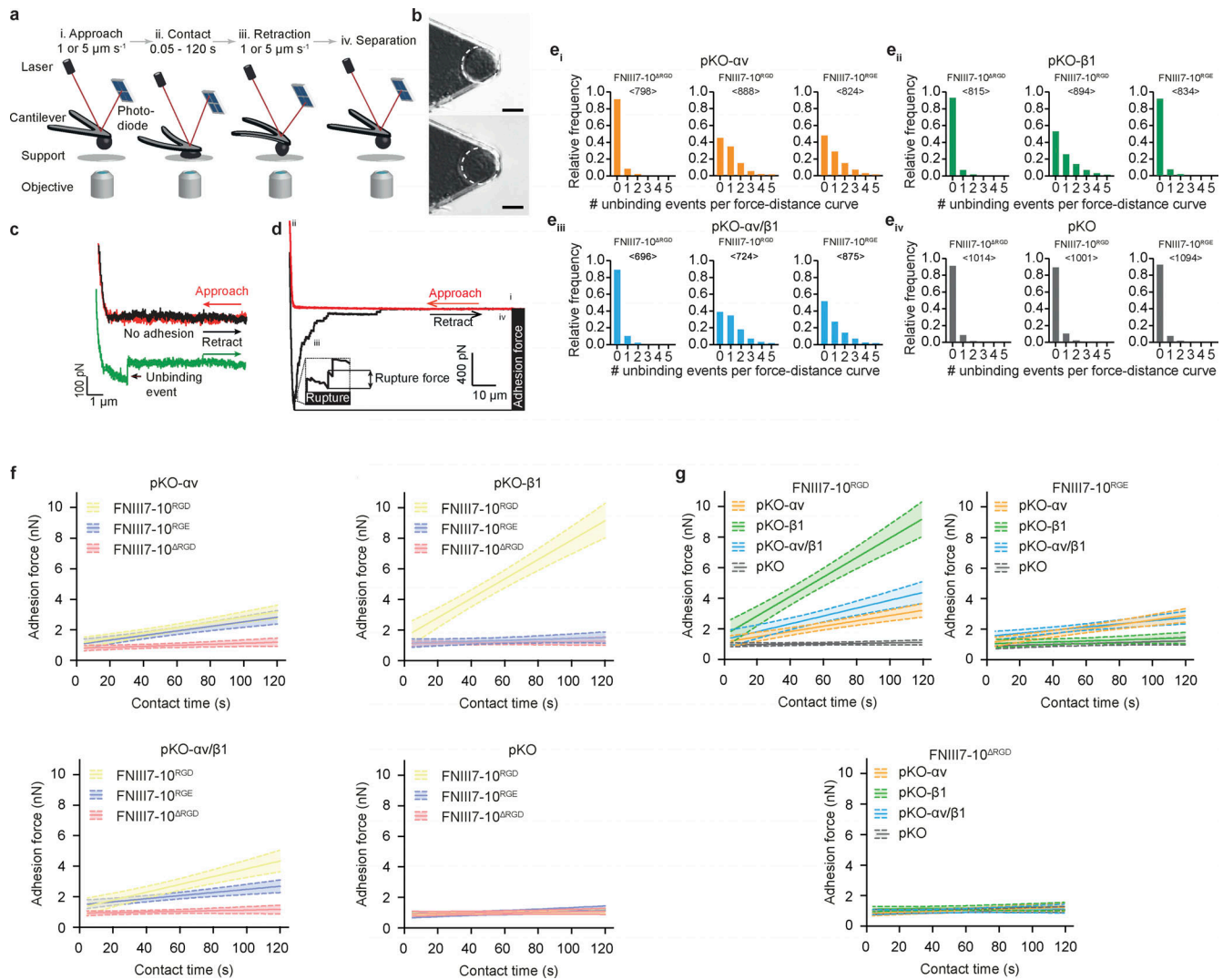
Figure S1. **AFM-based SCFS setup to quantify adhesion properties of fibroblasts to different full-length cFNs and FNIII7-10 fragments. (a)** SCFS setup. (i) Single fibroblasts are incubated for ~7–15 min on a concanavalin A–coated cantilever to assure firm attachment. (ii) Cantilever-attached fibroblasts are approached to cFN- or FN fragment–coated supports. (iii and iv) After 0–120 s contact time, the cantilever-bound fibroblast is retracted vertically until the fibroblast is fully detached from substrate to either quantify binding probabilities or measure adhesion force between fibroblast and support. During adhesion experiments, cantilever deflections are recorded and displayed in FD curves. **(b)** A single round fibroblast attached to the cantilever tip used to measurement adhesion forces (top) until the fibroblast's morphology changed (i.e., spreading; bottom). Scale bars, 10 µm. **(c)** FD curves representing binding of single integrins on fibroblasts to FN- or FNIII7-10–coated substrate. To record single integrin unbinding events, fibroblasts are approached to the substrate (red curve) until they contact the substrate at minimal contact force (200 pN) and contact time (~50 or ~300 ms) and are then retracted (black/green curve). The green FD curve shows a single adhesion (unbinding) event, while the black FD curve shows no adhesion event. **(d)** A representative FD curve after longer contact times (5–120 s) show different features; the retraction FD curve (black) records adhesion forces of the fibroblast, which represent the maximum downward deflection of the cantilever and thus the force required to separate the fibroblast from the substrate. During detachment of the fibroblast from the substrate, single receptor unbinding events are observed (ruptures). Ruptures are recorded when bonds formed between cytoskeleton-linked integrins and substrate fail. Tethers (longer force plateaus) are recorded when a membrane tether extrudes from the cell body with a single integrin or multiple integrins at its tip and occur when the integrin linkage to the actomyosin cytoskeleton is either too weak to resist the mechanical load applied or nonexistent. **(e)** The relative frequency distribution of unbinding events in single FD curves recorded for binding probability experiments with a contact time of ~300 ms for pKO-αv (i), pKO-β1 (ii), pKO-αv/β1 (iii), or pKO (iv) fibroblasts to FNIII7-10^ΔRGD, FNIII7-10^RGD, or FNIII7-10^RGE (FD curves taken from experiments from Fig. 1 c). <*n*> denotes the number of FD curves analyzed per condition. **(f and g)** Adhesion-strengthening dynamics for pKO-αv, pKO-β1, pKO-αv/β1, or pKO fibroblasts to FNIII7-10^ΔRGD, FNIII7-10^RGD, and FNIII7-10^RGE are shown. For each condition, a linear fit was used to fit all adhesion forces for all contact times (data taken from Fig 1, h–k). Lines depict the fit and dashed lines the 95% confidence interval of the fit. Adhesion-strengthening dynamics are quantified by the slope of the fit and are composed for each fibroblasts line (f) or FNIII7-10 fragments (g). Statistical tests for slope differences are listed in Table S1.
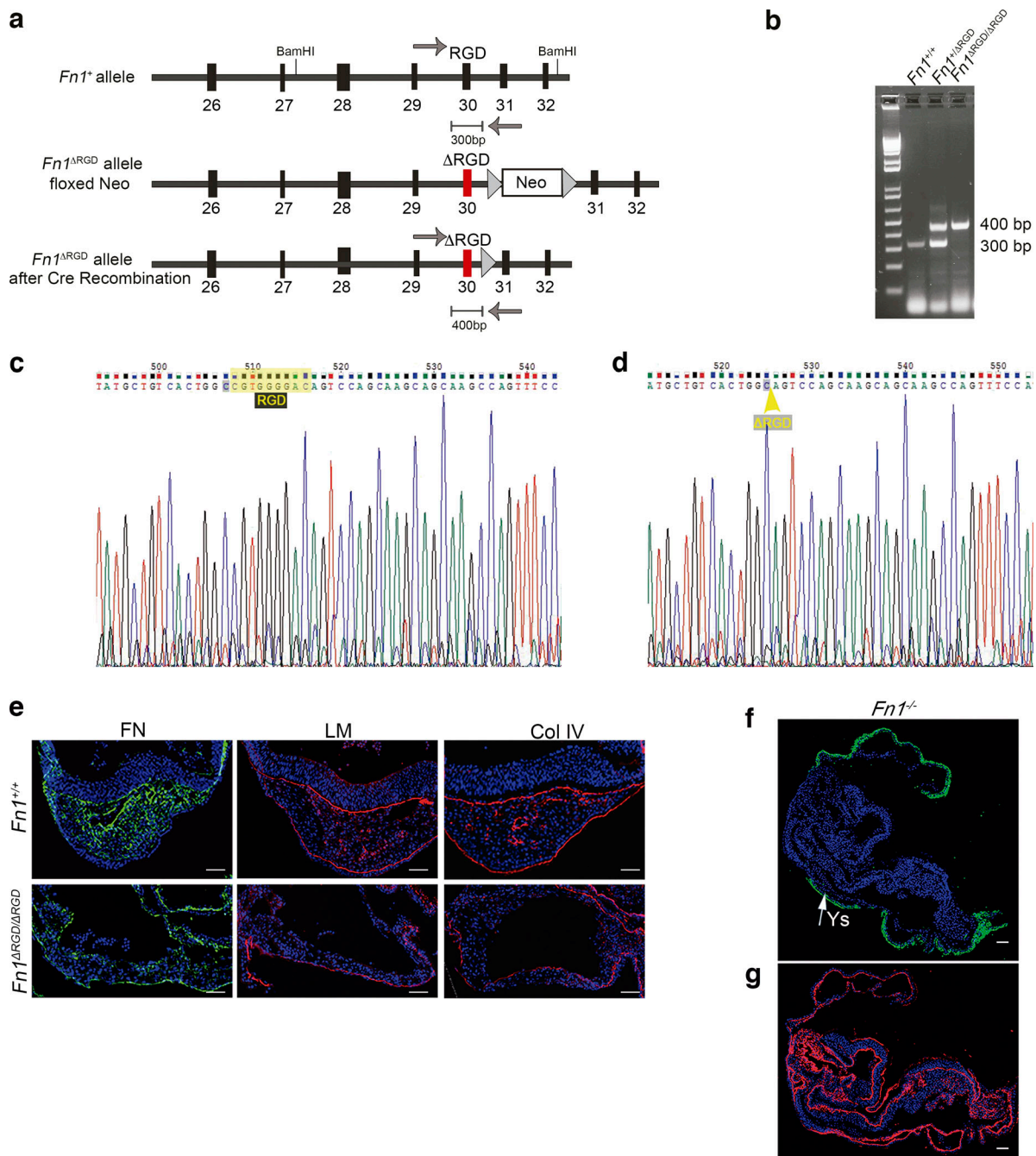
Figure S2. **Information to *Fn1^ΔRGD/ΔRGD* mouse generation and FN distribution in BMs and yolk sac from *Fn1^ΔRGD/ΔRGD* embryos. (a)** Strategy to generate *Fn1^ΔRGD/ΔRGD* mice. **(b)** PCR genotypes with primers indicated in panel a by arrows. **(c and d)** Nucleotide sequence of wild-type *Fn1* (c) and *Fn1^ΔRGD* allele (d) confirms RGD deletion. **(e)** Immunofluorescence of FN (green), laminin (LM; red), and collagen type IV (Col IV; red) in E9.5 *Fn1^+/+* and *Fn1^ΔRGD/ΔRGD* embryos. **(f and g)** Immunofluorescence of FN (green) and nidogen (red) in *Fn1^−/−* embryos. Arrow indicates FN in the yolk sac (Ys). Scale bars, 50 μm (e) and 200 μm (f and g).
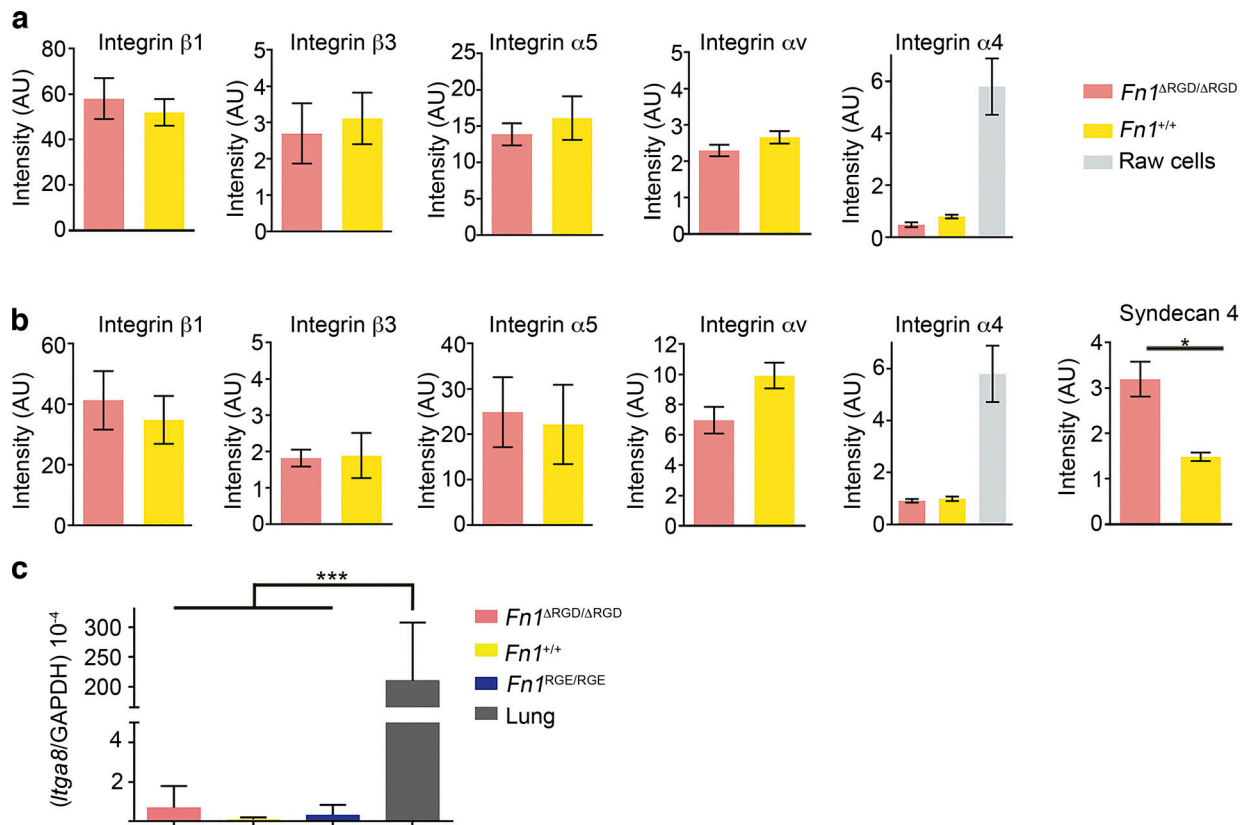
Figure S3. **Integrin expression. (a and b)** FACS-based measurements of integrin levels on the surface of *Fn1*^{+/+} and *Fn1*[ΔRGD/ΔRGD] ES cells (a) and integrin and syndecan 4 levels on *Fn1*^{+/+} and *Fn1*[ΔRGD/ΔRGD] fibroblasts (b). Intensities obtained with specific antibodies were normalized to isotype controls. Intensity values near 1 indicate that similar values were obtained with specific antibody and the isotype control. Raw cells were used as positive control for α4 integrin expression. Experiments were repeated three times, and 10,000 cells were analyzed per experiment. AU, arbitrary units. **(c)** Quantitative real-time PCR analysis of *Itga8* gene expression in *Fn1*[ΔRGD] fibroblasts with mRNA from mouse lung as a positive control. Data are from three independent experiments performed in triplicate (normalized to GAPDH). Bars represent mean ± SD of the average fold induction compared with mouse lung tissue. Statistical significances were calculated using two-tailed unpaired Student *t* tests; *, P < 0.05; ***, P < 0.001.
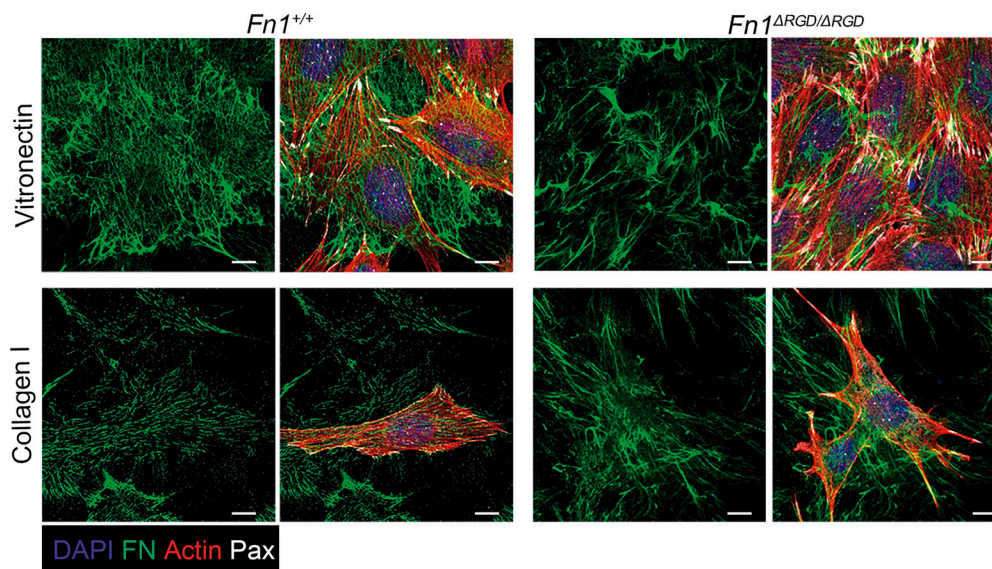

Figure S4. **FN[ΔRGD] assembly by cells cultured on VN or collagen I.** Fluorescence signal of FN (green), paxillin (Pax; white), F-actin (phalloidin; red), and nuclei (DAPI; blue) by *Fn1*^{+/+} and *Fn1*[ΔRGD/ΔRGD] fibroblasts seeded on either VN or collagen I for 24 h in SRM. Scale bars, 10 µm.
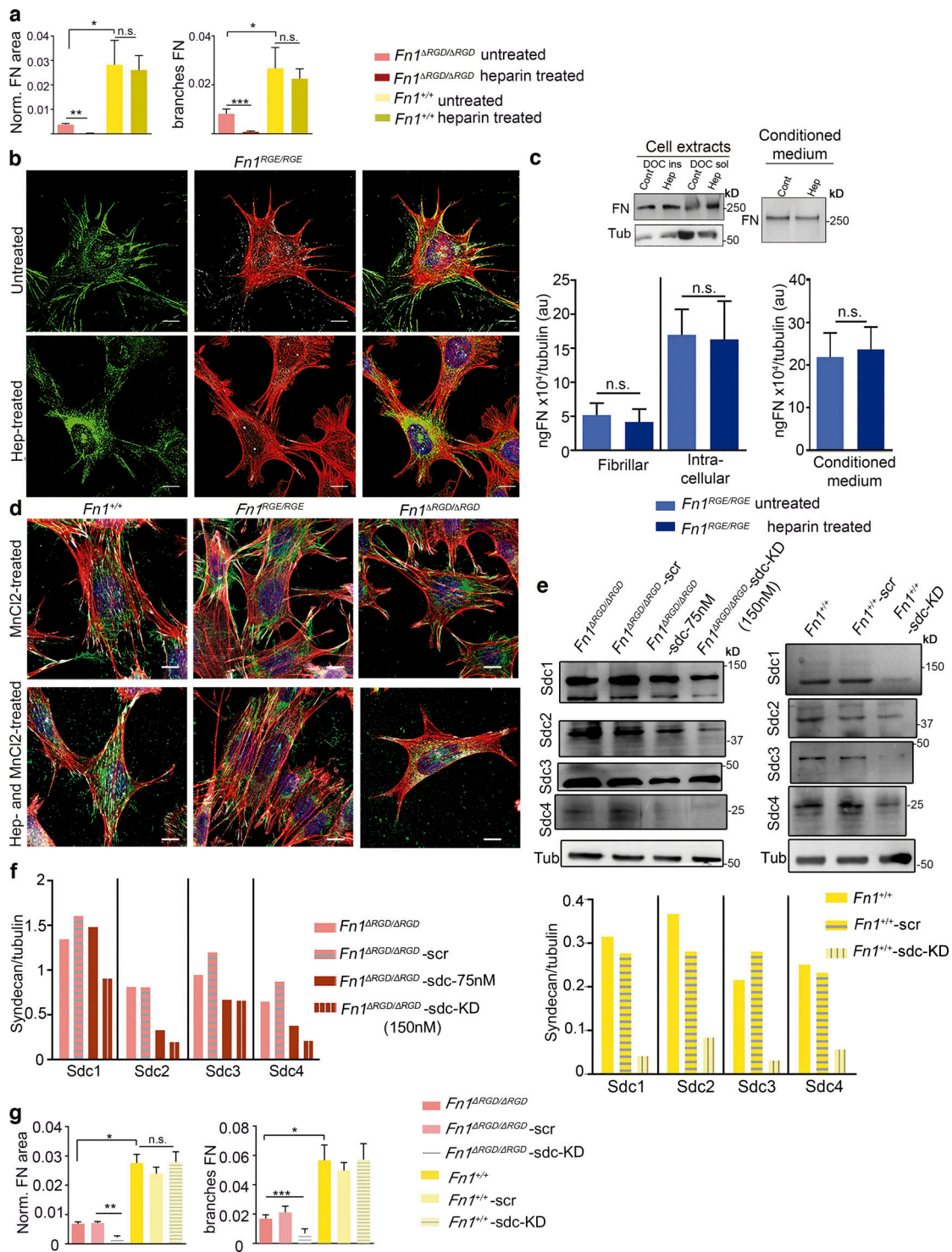
Figure S5. **FN^RGD, FN^RGE, and FN^ΔRGD assembly in the presence of heparin, Mn^+2, or syndecan siRNA and syndecan expression after knockdown.** **(a)** Quantification of FN^RGD and FN^ΔRGD fibril content and number of branched points in absence and presence of heparin after 24 h. Bars indicate mean (n = 20–30 cells per condition) and SEM. **(b)** FN assembly by $Fn1^{RGE/RGE}$ fibroblasts seeded on laminin and treated without or with heparin. FN, green; F-actin, red; paxillin, white; and DAPI, blue. **(c)** Representative WB and quantification of DOC-insoluble and DOC-soluble FN from cell extracts and FN in the conditioned culture medium without and with heparin treatment for 24 h. FN levels are shown relative to total tubulin in the cell extract. **(d)** FN^RGD, FN^RGE, and FN^ΔRGD assembly by $Fn1^{+/+}$, $Fn1^{RGE/RGE}$ and $Fn1^{ΔRGD/ΔRGD}$ fibroblasts, respectively, seeded on laminin and cultured in SRM with MnCl$_2$ or with MnCl$_2$ and heparin. FN, green; F-actin, red; paxillin, white; and DAPI, blue. **(e and f)** Representative WBs and quantification of syndecan 1–4 protein levels in $Fn1^{+/+}$ and $Fn1^{ΔRGD/ΔRGD}$ fibroblasts 96 h after transfection with siRNA to deplete syndecans. Syndecan protein levels were normalized to tubulin. **(g)** Quantification of FN^RGD and FN^ΔRGD fibril content and number of branched points after syndecan knockdown (sdc-KD) or in the presence of scr RNA. Bars indicate mean and SEM of three independent experiments. Statistical significances were calculated using two-tailed Student t tests and corrected with a Bonferroni post-hoc test; *, $P < 0.05$; **, $P < 0.01$; ***, $P < 0.001$; n.s., not significant. Scale bars, 10 μm. au, arbitrary units.

Table S1 is provided online as a Word document and shows a statistical comparison of adhesion-strengthening dynamics of pKO-αv, pKO-β1, pKO-αv/β1, and pKO cell lines to FNIII7-10$^{\Delta RGD}$, FNIII7-10^{RGD}, and FNIII7-10^{RGE}. Cross tables list P values for slope comparison of linear fits for adhesion-strengthening dynamics (shown in Fig. S1, f and g). P values were calculated from the indicated pairs of datasets using two-tailed F tests and are shown in bold if P < 0.05.